A Prototype Precipitation Retrieval Algorithm over Land for ATMS

YALEI YOU AND NAI-YU WANG

Earth System Science Interdisciplinary Center, and Cooperative Institute for Climate and Satellites, University of Maryland, College Park, College Park, Maryland

RALPH FERRARO

NOAA/NESDIS/STAR, College Park, Maryland

PATRICK MEYERS

Earth System Science Interdisciplinary Center, and Cooperative Institute for Climate and Satellites, University of Maryland, College Park, College Park, Maryland

(Manuscript received 1 September 2015, in final form 26 January 2016)

ABSTRACT

A prototype precipitation algorithm for the Advanced Technology Microwave Sounder (ATMS) was developed by using 3-yr coincident ground radar and ATMS observations over the continental United States (CONUS). Several major improvements to a previously published algorithm for the Special Sensor Microwave Imager/Sounder (SSMIS) include 1) considering the different footprint size of ATMS pixels, 2) calculating the uncertainty associated with the precipitation estimation, and 3) extending the algorithm to the 60°S–60°N region using only CONUS observations to construct the database. It is found that the retrieved and radar-observed rain rates agree well (e.g., correlation 0.66) and the one-standard-deviation error bar provides valuable retrieval uncertainty information. The geospatial pattern from the retrieved rain rate is largely consistent with that from radar observations. For the snowfall performance, the ATMS-retrieved results clearly capture the snowfall events over the Rocky Mountain region, while radar observations almost entirely miss the snowfall events over this region. Further, this algorithm is applied to the 60°S–60°N land region. The representative nature of rainfall over CONUS permitted the application of this algorithm to 60°S–60°N for rainfall retrieval, evidenced by the progress and retreat of the major rainbands. However, an artificially large snowfall rate is observed in several regions (e.g., Tibetan Plateau and Siberia) because of frequent false detection and overestimation caused by much colder brightness temperatures.

1. Introduction

Passive microwave observations have more direct physical relation with the hydrometers in the atmosphere relative to infrared and visible observations, which capture the cloud-top features (Barrett and Beaumont 1994; Petty 1995; Kidd and Levizzani 2011). Therefore, precipitation estimates from passive microwave radiometers are more accurate and are essential for accuracy of satellite-based, high-resolution, near-global precipitation datasets (Hou et al. 2014; Yong et al. 2015), for example, the Tropical Rainfall Measuring Mission (TRMM) Multisatellite Precipitation Analysis (TMPA; Huffman et al. 2007), National Oceanic and Atmospheric Administration (NOAA) Climate Prediction Center (CPC) morphing technique (CMORPH; Joyce et al. 2004), Global Satellite Mapping of Precipitation (GSMaP; Kubota et al. 2007), and Precipitation Estimation from Remotely Sensed Information Using Artificial Neural Networks (PERSIANN; Ashouri et al. 2015). In fact, the precipitation estimation from infrared is adjusted using passive microwave observations in the aforementioned four near-global level-3 products.

Passive microwave radiometers can be grouped into two scanning schemes: 1) conical-scanning imagers [e.g., TRMM Microwave Imager (TMI) and Global

Corresponding author address: Yalei You, ESSIC, University of Maryland, College Park, 5825 Research Court, College Park, MD 20740.
E-mail: yyou@umd.edu

DOI: 10.1175/JHM-D-15-0163.1

Precipitation Measurement (GPM) Microwave Imager (GMI)] and 2) cross track–scanning sounders [e.g., Advanced Microwave Sounding Unit (AMSU) and Advanced Technology Microwave Sounder (ATMS)]. For conical-scanning imagers, the footprint size and polarization remain constant regardless of the position of the pixel in the scan line, which simplifies the radiative transfer modeling. In contrast, the footprint size, the polarization, and the orientation differ for each scan position for cross track–scanning radiometers. The sounders are primarily responsible for the retrieval of the moisture and temperature profiles because of the availability of channels sensitive to water vapor, oxygen, and carbon dioxide (Grody 1993). Researchers have historically focused more on the precipitation retrieval algorithm development for imagers. For example, numerous algorithms, either using regression model or Bayesian technique, have been developed for the Special Sensor Microwave Imager (SSM/I) and Special Sensor Microwave Imager/Sounder (SSMIS; e.g., Spencer et al. 1989; Liu and Curry 1992; Petty 1994; Ferraro and Marks 1995; McCollum and Ferraro 2003; Sanò et al. 2013; You et al. 2015). Similarly, a variety of the precipitation retrieval algorithms have also been developed for TMI, including Kummerow et al. (2001), Viltard et al. (2006), Wang et al. (2009), Aonashi et al. (2009), Gopalan et al. (2010), Islam et al. (2015), and Ebtehaj et al. (2015). The newly developed (2014 version) fully parametric Goddard profiling algorithm (GPROF2014) has been successfully applied to all GPM constellation imagers, while extending this framework to sounders is still in progress (Kummerow et al. 2015).

Less work has been done for the sounders, partially because of the designed purpose, varying footprint size, and mixed polarization off nadir. However, the precipitation estimations from sounders are indispensable to produce an accurate 3-h global precipitation map. In fact, about half of the passive microwave sensors in GPM constellation radiometers are cross track–scanning sounders [e.g., AMSU-A, AMSU-B, Microwave Humidity Sounder (MHS), and ATMS]. Several pioneering studies have been conducted to detect and retrieve the precipitation using the sounders. The Microwave Surface and Precipitation Products System (MSPPS) has been updated since 1995 at NOAA's National Environmental Satellite, Data, and Information Service (NESDIS) to retrieve operational near-real-time surface and precipitation products (e.g., total precipitable water, ice water path, rain rate, and surface temperature) using AMSU data. The MSPPS retrieval algorithms for each surface and precipitation variable were later documented by Grody et al. (2001), Weng et al. (2003), Kongoli et al. (2003), and Ferraro et al. (2005). A regression model converts the ice water path to a surface rain rate, where the coefficients are obtained using cloud model results and vary for different cloud systems (e.g., stratiform vs convective; Ferraro et al. 2000). Several validation studies showed that the MSPPS-retrieved rain rate agrees well with ground observations (Ferraro et al. 2000; Qiu et al. 2005; Vila et al. 2007). A similar method (i.e., converting water paths to surface rain rate) was adopted by the Microwave Integrated Retrieval System (MIRS; Boukabara et al. 2011), which is currently implemented operationally to multiple sounders (including AMSU and ATMS) at NOAA. The MIRS is designed to estimate a comprehensive set of atmospheric and surface parameters (e.g., ice water path, liquid water path, cloud water, and emissivity) simultaneously from microwave measurements based on the 1D variational approach. Detailed implementations of this algorithm to ATMS are described by Boukabara et al. (2013).

Staelin and Chen (2000) and Chen and Staelin (2003) utilized coincident observations of AMSU/MHS brightness temperature (TB) and ground radar observations over the United States to retrieve precipitation (both rainfall and snowfall) using only the opaque channels (54 and 183 GHz) to largely avoid the surface contamination. It is demonstrated from case studies that this algorithm captures the major characteristics from both rainfall and snowfall. A two-stream radiative transfer model and a cloud-resolving mesoscale numerical weather prediction model have been utilized by Surussavadee and Staelin (2008a) to simulate 122 global storms over both land and ocean at AMSU frequencies. The global precipitation rate is retrieved using 122 global storms simulations as the database through the neural network method. The retrieval results roughly agree with those from MSPPS (Surussavadee and Staelin 2008b). Surussavadee and Staelin (2010) later adapted this framework to ATMS, showing that large improvements have been made for the retrieved precipitation rate because of the finer pixel resolution, compared with AMSU. Laviola and Levizzani (2011) developed a fast rain-rate retrieval algorithm for AMSU-B and MHS, which mainly utilized the water vapor strong lines around 183 GHz. Convective and stratiform rainfall systems are separated by the TB difference between 89 and 150 GHz. The results from this algorithm show good agreement with that from the GPROF TRMM algorithm. Recently, a neural network approach was applied to AMSU/MHS observations by Sanò et al. (2015), and case studies demonstrate that the retrieved precipitation is in good agreement with ground radar and rain gauge observations.

Several previous studies compared the quality of the rainfall estimation from sounders and imagers. Lin and Hou (2008) comprehensively assessed the surface rain retrieval from a cross track–scanning microwave sounder (AMSU-B) and conical-scanning microwave imagers [TMI, Advanced Microwave Scanning Radiometer for Earth Observing System (AMSR-E), and SSM/I]. Rainfall estimation characteristics from AMSU-B over land between 1.0 and 10.0 mm h^{-1} are similar to those from conical-scanning radiometers. However, for instantaneous rainfall lighter than 1 mm h^{-1} and heavier than 10 mm h^{-1}, the performance of the imager is noticeably better. Wolff and Fisher (2009) and Fisher and Wolff (2011) showed that AMSU-B exhibited the least skill relative to ground observations over two TRMM ground validation sites, compared with three imagers (SSM/I, AMSR-E, and TMI). Significant efforts have been made to compare the precipitation retrieval results from 12 passive microwave radiometers, including six imagers and six sounders (Tang et al. 2014). The imagers produce more accurate precipitation retrievals relative to the sounders, which tend to have a narrower dynamic rainfall range, higher biases, and random errors. Because of the relatively worse performance of the sounders, TMPA, version 7, uses fewer sounder observations than in its prior version and prioritizes imager retrievals over sounders when there are multiple observations in a single grid box (Yong et al. 2015).

Considering the extensive daily coverage by sounders but their relatively poor precipitation retrieval performance, a new algorithm is necessary. Previous work established a prototype Bayesian algorithm for SSMIS that is stratified by ancillary information on surface conditions and the vertical structure of precipitation (You et al. 2015). This algorithm greatly outperforms the traditional single-database algorithm. The primary objective of this study is to extend this algorithm to ATMS. Compared with previously published ATMS precipitation algorithms (Surussavadee and Staelin 2010; Boukabara et al. 2013), the unique features of this algorithm include 1) alleviating the ill-posed inversion retrieval problem by stratifying the single database into many smaller but more homogeneous databases (in this study, there are 30 smaller databases for rainfall retrieval and 12 smaller databases for snowfall retrieval); 2) employing a Bayesian framework, compared with the neural network (Surussavadee and Staelin 2010) and regression (Boukabara et al. 2013) approaches; and 3) simultaneously retrieving the instantaneous precipitation rate and the associated uncertainties. Further, we will demonstrate that a database populated with observations over the continental United States (CONUS) can be easily expanded to the global scale by using physically meaningful parameters.

2. Data

This section describes the primary datasets used in this work, including ground radar precipitation observations over the CONUS and the satellite observations from ATMS. It also discusses several ancillary datasets, including surface type derived from climatological emissivity, Modern-Era Retrospective Analysis for Research and Applications (MERRA) data, NOAA 1-km elevation data, the National Climatic Data Center (NCDC) integrated surface database (ISD), and the Global Precipitation Climatology Centre (GPCC) monthly precipitation dataset.

a. National Mosaic and Multi-Sensor Quantitative Precipitation Estimation

In this study, the 5-min (2 min since August 2013), 1-km gridded National Mosaic and Multi-Sensor Quantitative Precipitation Estimation (NMQ) data (Zhang et al. 2011b) are taken as the ground reference. To account for errors from terrain blockage and radar brightband influence, a radar quality index (RQI) from 0 to 1 is provided for each precipitation estimation at each grid point, with 1 indicating the highest-quality data. In general, the RQI is smaller in complex terrain than in flatlands and smaller in areas with low freezing levels compared to those with high freezing levels (Zhang et al. 2011a). In this study, only precipitation estimates with an RQI larger than 0.5 are used to construct the precipitation (rainfall and snowfall) databases. This threshold value (0.5) is taken by considering the trade-off between the sample size and the quality of radar precipitation estimates. Using this threshold, about 80% of the rainfall estimations are kept, while only about 40% of the snowfall estimations are kept. It is noted that the RQI is positively related with the precipitation intensity. Choosing this threshold (0.5) filtered out some light precipitation rate.

Several validation studies evaluated the NMQ rainfall performance (e.g., Wu et al. 2012; Chen et al. 2013; Tang et al. 2014). There are positive biases in the NMQ rainfall estimates in the central United States, compared with gauge observations and gauge-corrected radar observations. However, this product has very high temporal resolution, which ensures that enough collocated samples with ATMS are obtained. We would like to emphasize that it is not our purpose to consider the NMQ as the ground truth. Instead, we use this product to demonstrate our prototype algorithm for ATMS. There are few evaluations regarding the NMQ snowfall

rate. In this study, we have conducted a preliminary snowfall rate comparison between surface gauge observations from ISD and NMQ radar estimations.

b. Advanced Technology Microwave Sounder

As the follow-on instrument to the AMSU and MHS, the ATMS instrument on board the *Suomi–National Polar-Orbiting Partnership* (*Suomi-NPP*) satellite was successfully launched in October 2011, which scans cross-track ±52.8° relative to nadir at 824-km altitude (Kim et al. 2014). There are 22 channels from ATMS, and 96 field-of-view (FOV) samples are taken for each scan line. In this study, 13 channels that are closely related to the precipitation process are used. They are 23.8 [quasi-vertical polarization (QV)], 31.4 (QV), 50.3 [quasi-horizontal polarization (QH)], 51.2 (QH), 52.8 (QH), 53.596 ± 0.115 (QH), 88.2 (QV), 165.5 (QH), 183.31 ± 1 (QH), 183.31 ± 1.8 (QH), 183.31 ± 3 (QH), 183.31 ± 4.5 (QH), and 183.31 ± 7 (QH) GHz. Hereafter, these channels will be referred to as V24, V31, . . . , and H183.3 ± 7 for convenience. The horizontal resolution at nadir is approximately 72 km for the 24- and 31-GHz channels, 32 km for channels up to 88 GHz, and 16 km for the 166-GHz channel and higher-frequency channels. The pixel size increases dramatically from the center of the scan line to the edge. For example, the FOV size at nadir at V88 is about 32 km, while it is 136 × 60 km at the edge of the swath. The varying pixel size needs special treatment for precipitation retrieval, as discussed in section 4.

c. Ancillary datasets

Five ancillary datasets are utilized in this study, including surface type data, MERRA data, GPCC monthly precipitation data, and hourly surface gauge observations. A brief description for each dataset is provided below.

Aires et al. (2011) developed a Tool to Estimate Land Surface Emissivities at Microwave frequencies (TELSEM) based on the clear-sky microwave emissivities. These emissivity values are further condensed into 11 surface types to largely capture the surface characteristics in the microwave frequency. The monthly surface type index is put at 0.25° spatial resolution. The relative humidity, vertical velocity, geopotential height, and temperature profiles from MERRA are provided every 3 h at approximately 0.5° resolution. Hourly surface temperature and 2-m air temperature T_{2m} are also extracted from MERRA. The 1-km terrain elevation data are provided by NOAA (Hastings and Dunbar 1998). The GPCC monthly precipitation data are a gridded gauge-analysis product derived from quality-controlled station data (Schneider et al. 2014). The latest version [version 4 (V4)] of the monthly GPCC monitoring product with the 1° × 1° spatial resolution will be used as a reference to compare with the ATMS-derived rain rate over the 60°S–60°N land region.

The precipitation type (snow vs rain) information is obtained from the NCDC integrated surface hourly observations (Smith et al. 2011). Significant efforts are made to compile the hourly precipitation observations from numerous sources (including regular weather reports and automated weather stations) into a single common dataset. A systematic quality-control procedure is applied to all data to ensure consistency between parameters and continuity between observations. This dataset is generally regarded as the ground "truth" and has been used in studies examining precipitation trend analysis (Dai et al. 1997), extreme events monitoring (Vose et al. 2014), precipitation phase separation (Dai 2008; Kongoli et al. 2015), and satellite product validation (Linden et al. 2015). In this study, this dataset is used to develop a snow–rain separation method for satellite retrieval purposes and to validate the radar-observed snowfall rate.

There are three spatial resolutions for the 13 ATMS channels. The FOV at nadir is approximately 16 km for 166 GHz and higher-frequency channels, 32 km for channels between 50 and 88 GHz, and 72 km for the lower-frequency channels (24 and 31 GHz). The resolution at V88 is taken as the nominal resolution. The four closest pixels at higher frequencies from 166 GHz to 183.3 ± 7 GHz are chosen since the area occupied by these four pixels is approximately the same as the FOV of the 88-GHz channel (e.g., at nadir, $32^2/16^2 = 4$), and then the TBs from these four pixels are simply averaged to represent the corresponding TBs at the 88-GHz resolution. For lower-frequency channels (i.e., 24 and 31 GHz), their original coarser spatial resolution has been used in this study. That is, the closest neighbor pixel to the V88 pixel is chosen. This collocation process is conceptually similar to that of Viltard et al. (2006). Since the TB resolution at 88 GHz varies along the scan line, the corresponding NMQ precipitation rate at the 88-GHz nominal resolution is calculated by averaging the closest N precipitation rate values to the V88 resolution. The closest N NMQ observations are those in a circle with different radii from center to edge. At nadir, the radius is 32 km for 88 GHz. However, off nadir, the shape of the footprint becomes an ellipse. The ellipse shape of the footprint off nadir is approximately taken as a circle where the radius is assumed to be $\sqrt{r_1 \times r_2}$ (where r_1 and r_2 are the major and minor axes, respectively). For example, the closest 1024 ($N = 32 \times 32$) NMQ 1-km grid points to each V88 pixel are averaged in the center of the scan line, while the closest 8220

(137 × 60) are averaged at the edge of the scan line. On average, the precipitation rate at the edge is inevitably smaller than that over the center because the averaging is taking place over a much larger area. For all other data (surface type, surface temperature, and land elevation), we use data from the closest grid. Surface temperature, vertical velocity, relative humidity, and temperature profiles are linearly interpolated to match the time of the TB observation.

The database is constructed using coincident ATMS and NMQ measurements from 2012 to 2013, while collocated data from 2014 are used for algorithm validation. The MIRS retrieval result for ATMS is available on the NOAA Comprehensive Large Array-Data Stewardship System (CLASS; http://www.class.ngdc.noaa.gov) from April 2014 and is used as a benchmark. Retrieved rain rates are also compared to the GPCC gauge-analysis dataset.

3. Methodology

Two major statistical approaches (linear discriminant analysis and Bayesian framework) in You et al. (2015) will be used in this study and are briefly summarized here.

Linear discriminant analysis (LDA) is used for precipitation detection. The LDA approach condenses a large number of variables into a single variable while keeping as much discriminatory information as possible. Turk et al. (2014) showed that the LDA method outperforms the widely used scattering index method (Grody 1991) for rainfall detection, especially in winter months. The 13 TBs are combined into a single discriminant index (DI) for rainfall detection. You et al. (2015) demonstrated that including the vertical velocity at 700 hPa and average relative humidity from 1000 to 700 hPa improved the snowfall detection performance by as much as 20%. Similar findings were reported by Behrangi et al. (2015). Therefore, the vertical velocity, relative humidity, and the 13 TBs are included in the LDA process for snowfall detection. The probability of detection for rainfall and snowfall is 0.86 and 0.72, respectively.

The widely used Bayesian method (e.g., Evans et al. 1995; Kummerow et al. 1996; Seo and Liu 2005; Chiu and Petty 2006; Noh et al. 2006; Kim et al. 2008; Sanò et al. 2013; Petty and Li 2013) in the precipitation/cloud retrieval community can be mathematically stated as follows:

$$f(x\,|\,\mathbf{T}) = \frac{f(\mathbf{T}\,|\,x)\times f(x)}{f(\mathbf{T})} = \frac{f(\mathbf{T}\,|\,x)\times f(x)}{\int f(\mathbf{T}\,|\,x)\times f(x)\,dx}, \tag{1}$$

where x and $\mathbf{T}$ represent precipitation rate and TBs, respectively; $f(x\,|\,\mathbf{T})$ is the posterior probability density function (PDF) of x given the measured $\mathbf{T}$; $f(x)$ is the prior PDF of x; and $f(\mathbf{T}\,|\,x)$ is the likelihood function of $\mathbf{T}$ given the precipitation rate x.

Similar to Kummerow et al. (1996), the expected value of x is obtained without knowing the analytical form of the posterior PDF. In addition, principal component analysis (PCA) is applied to the 13 TBs, and only the first three principal components (PCs; about 98% total variance explained) are used in the Bayesian framework, which ensures the covariance matrix is diagonal. Compared to You et al. (2015), a major improvement of this work is that the variance (an uncertainty metric) corresponding to each precipitation estimate is calculated, similar to Evans et al. (2002). The expected value of x and its corresponding variance are computed in the following way:

$$E(x\,|\,\mathbf{u}) = \frac{\int x\times f(\mathbf{u}\,|\,x)\times f(x)\,dx}{\int f(\mathbf{u}\,|\,x)\times f(x)\,dx} = \frac{E[x\times f(\mathbf{u}\,|\,x)]}{E[f(\mathbf{u}\,|\,x)]} \quad \text{and} \tag{2}$$

$$\mathrm{Var}(x\,|\,\mathbf{u}) = \int [x - E(x\,|\,\mathbf{u})]^2 f(x\,|\,\mathbf{u})\,dx, \tag{3}$$

where $\mathbf{u}$ is the TB principal components, and E and Var stand for the expectation and variance, respectively.

The nonraining pixels judged by the LDA approach are not included in the Bayesian calculation process. It is pointed out by Seo et al. (2007) and Seo et al. (2008) that this causes the overestimation for the light rain rate (<1 mm h^{-1}) and leads to a slightly larger average rain rate. In our current work, it is difficult to directly estimate the nonraining pixel numbers over the 60°S–60°N region except over CONUS. Second, adding the nonraining pixels may lead to underestimation for the heavy rainfall under certain situations. For example, the TBs do not decrease significantly for heavy precipitation from the warm rain systems because of the weak scattering signature. Under this scenario, the vast majority of the nonraining TBs will have negative impact (underestimation) for the retrieved rain rate. In addition, as pointed out by Seo et al. (2008) and demonstrated by GPROF2014, directly adding the nonraining pixels into the database will lead to a positive precipitation rate for every new observation. For these reasons, we decided to screen the precipitation first and then apply the Bayesian approach to retrieve precipitation.

Following You et al. (2015), the collocated TBs and precipitation rate are first grouped into many smaller

databases using four parameters (surface type, surface temperature, land elevation, and ice layer thickness). Similar to Aonashi et al. (2009), the TB difference (V24 − V88) is utilized to estimate the storm-top height through a regression model. The ice layer thickness is the difference between storm-top height and freezing-level height (FLH), where FLH is obtained from the MERRA dataset. These four parameters effectively reduce the TB variations corresponding to the same surface rain rate and thus alleviate the ill-posed inversion issue (You et al. 2015). In each stratified database, the LDA approach is used to judge whether a pixel is associated with rainfall (snowfall). If a pixel is deemed as rain pixel or snow pixel, the Bayesian technique is utilized to obtain the precipitation rate. Otherwise, the corresponding precipitation rate is assigned as $0\,\mathrm{mm\,h^{-1}}$.

The database stratification and precipitation retrieval framework is conceptually similar to GPROF2014 (Kummerow et al. 2015). However, this algorithm differs from GPROF2014 in three main aspects: 1) the surface type, surface temperature, land elevation, and ice layer thickness are used in this study to stratify the database, while surface type, surface temperature, and total precipitable water (TPW) are used in GPROF2014; 2) the Bayesian search is conducted in PC space in this study and TB space in GPROF2014; and 3) the PC variance matrix is precipitation intensity dependent in this study while the TB covariance matrix is constant in GPROF2014.

4. Brightness temperature variation along the scan line

The TB variation at each pixel position along the scan line is investigated over three regions with relative uniform surface background: the Amazon forest (7.5°S–2.5°N, 60°–70°W), the Sahara Desert (5°–15°N, 20°E–30°W), and the southern Great Plains in the United States (SGP; 30°–40°N, 90°–100°W). Only noncloudy pixels are selected to avoid the possible cloud and precipitation contamination. The noncloudy pixels are simply defined as scenes where the TB difference between H183 ± 7 and H183 ± 3 is greater than 10 K. Moradi et al. (2013) concluded that this threshold is very strict and ensures that almost all the cloudy pixels are filtered out.

Figure 1 shows the TB variations at V24, V88, and H183 ± 7 over these three selected regions. Regardless of the frequency and geolocation, the TBs at the edges of the scan line are lower than those in the center of the scan line. This is a result from the combined effects of surface emissivity, varying polarization, and different traveling distances in the atmosphere (Yang et al. 2013). Specifically, the TBs are about 5 K lower at the edges of the scan line (beam position from 1 to 20 and 77 to 96) than those in the center of the scan line (beam position from 21 to 76) over Amazon and SGP, except for the V24 over Amazon. The very dense vegetation possibly contributes to the smaller differences between the edge and center (about 2 K) at V24 over Amazon. For the Sahara Desert region, the TB difference between the edge and center, regardless of the channel frequencies, is about 8 K. Similar to the AMSU instrument, ATMS also shows some minor asymmetric effects across the scan line (Weng et al. 2003), which are more evident over the SGP than the Amazon and Sahara.

In summary, it is noticed that, regardless of the channel frequencies and the geolocations, the TBs at the edges of scan line are several degrees lower than those from the center. To account for this phenomenon in the retrieval algorithm, there are three approaches in the literature: 1) the brightness temperatures are ''corrected'' to values that would have been seen at nadir through radiative transfer simulation or statistical relation (e.g., Surussavadee and Staelin 2008a); 2) a correction factor is added in the final retrieved results, for example, an empirical relationship is established between local zenith angle and ice water path in the MSPPS (e.g., Ferraro et al. 2005); and 3) the pixels are grouped into different categories using their scan positions (e.g., Liu and Seo 2013). In this study, the third approach is selected. Ideally, one would treat each of the 96 scan positions differently and group these pixels into 96 categories. In reality, it is difficult to obtain enough observations to populate these 96 categories. In this work, only the edge pixels (beam positions 1–20 and 77–96) and center pixels (beam positions 21–76) are separated. That is, databases will be built for edge and center pixels separately.

5. Rain and snow separation

It is necessary to construct separate databases for rain and snow because they have very different radiometric signatures (Sims and Liu 2015). It has long been recognized that either phase of precipitation (rain or snow) can occur when the surface temperature is within a few degrees of freezing (e.g., Wagner 1957; Auer 1974; Bourgouin 2000; Dai 2008; Ye et al. 2013; Sims and Liu 2015). As expected, these studies demonstrated that the most dominant factor for snow–rain separation is the air temperature. Several studies (Wagner 1957; Dai 2008) also noticed that the snow–rain transition temperature also depends on the land elevation. Other factors, including relative humidity and temperature lapse rate, may also affect the snow–rain transition (Sims and Liu 2015).

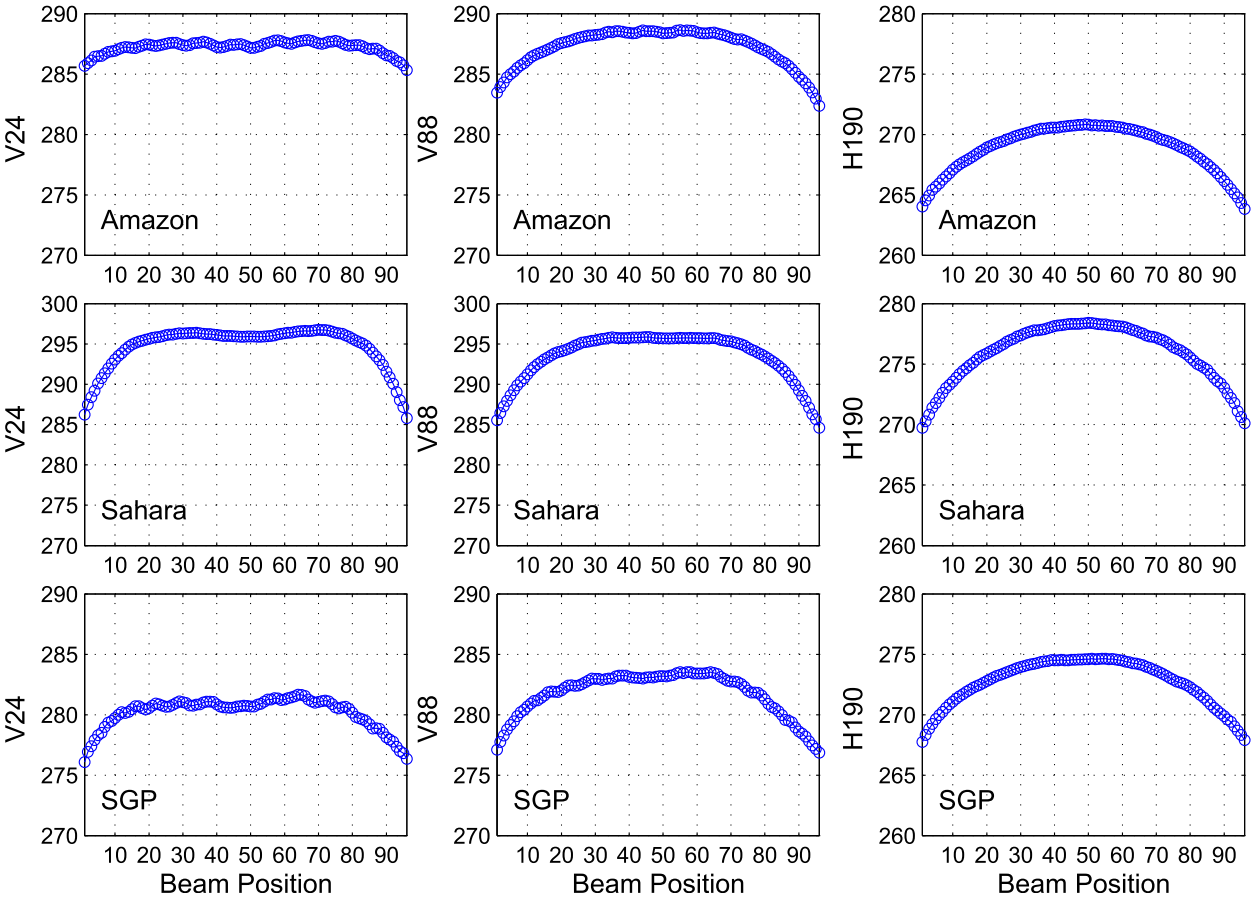

FIG. 1. The TB variations at V24, V88, and H183 ± 7 along the scan line over three selected regions, including Amazon forest (7.5°S–2.5°N, 60°–70°W), Sahara Desert (5°–15°N, 20°E–30°W), and SGP (30°–40°N, 90°–100°W).

In this study, only the two most dominant factors (elevation and air temperature) are considered. Hourly surface weather observations of precipitation type and 2-m air temperature from MERRA over the CONUS from 1979 to 2014 are used to determine the snowfall probability. This period of time (1979–2014) is chosen because of the availability of MERRA data. Unlike previous work (e.g., Dai 2008; Ye et al. 2013; Sims and Liu 2015), this study attempts to find the snow–rain transition threshold directly using the 2-m air temperature from MERRA data. Of course, the station-observed surface temperature is preferable to determine the snow–rain transition. In fact, it will be demonstrated in Fig. 2 that it is more effective to separate rain and snow using the station-observed surface temperature. However, there are often no station observations geographically close enough to the satellite pixels, which is particularly true over the station-sparse regions (e.g., Rocky Mountains, Siberia, and the Tibetan Plateau), which makes it impossible to collocate the station observations to satellite observations. For this specific reason, the MERRA 2-m air temperature, instead of the station-observed surface temperature, is used as the predictor for the snow–rain transition.

The likelihood of snowfall under different surface elevation scenarios using the station-observed surface temperature clearly shows that the snowfall probability is larger corresponding to the same surface temperature in the higher-elevation regions (Fig. 2a). In other words, snow could occur in a relatively warm environment in the higher-elevation areas. For example, corresponding to the 0.5 snowfall probability, the surface temperature is about 1.5°C over areas with elevations less than 1 km, while it is about 2.5°C over areas with elevations higher than 2 km. With a thinner air and lower air pressure over the high-elevation region, the snowflakes in the atmosphere tend to fall faster because of less drag force, and therefore they can keep their original type even in a relatively warm environment (Ye et al. 2013). The increasing temperature threshold for snow–rain transition over the high-elevation region has also been noticed by Dai (2008) and Ding et al. (2014).

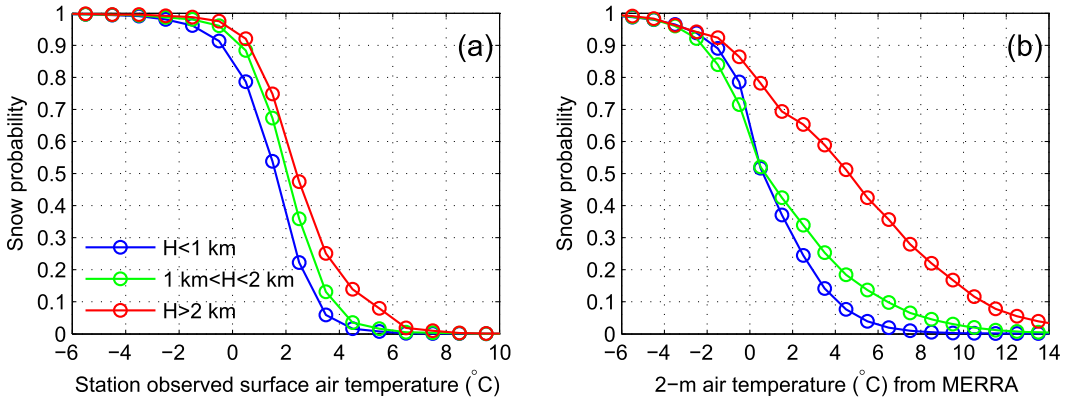

FIG. 2. (a) Snowfall probability corresponding to different station-observed surface temperatures over three elevation scenarios. (b) Snowfall probability corresponding to different 2-m air temperatures from MERRA. The correspondence between curve color and the elevation scenario is shown in (a).

Next, the snowfall probability is calculated using the MERRA 2-m air temperature in the same three elevation scenarios (Fig. 2b). Unlike the station-observed surface temperature, the snowfall probability is almost identical when the 2-m air temperature is colder than 2°C over regions with elevations lower than 2 km (blue and green curves in Fig. 2b). However, a much higher temperature threshold is evident over the regions with elevations higher than 2 km. To separate rain from snow, it is clear that the narrower the transition region, the more accurate the discriminant result will be. The narrower transitional region in Fig. 2a again demonstrates the superior performance of the station-observed surface temperature for snow–rain separation. As previously stated, station-observed surface temperature is preferable for snow–rain determination; however, the sparse station network requires reliance on the MERRA data.

Similar to previous studies (e.g., Dai 2008; Sims and Liu 2015), the 2-m air temperature threshold corresponding to the 50% snowfall probability is chosen as the separation threshold. The threshold temperature for regions with elevations below 2 km is 0.65°C and for regions with elevations higher than 2 km is 4.6°C (Fig. 2b).

6. Gauge-observed snowfall rate versus NMQ snowfall rate

As previously mentioned, the NMQ rain-rate performance has been extensively evaluated using gauge and gauge-corrected radar observations. The performance of the NMQ snowfall rate estimation has not yet been evaluated. In this study, a preliminary comparison between gauge observations and NMQ estimates is performed. Hourly snowfall rate observations are taken from the NCDC integrated surface hourly dataset. Only the gauge observations over approximately 482 first-order stations in 2014 are included. A first-order station is a site at which weather observations were taken by National Weather Service employees or other certified observers. These snow reports were also used by Kongoli et al. (2015) to derive the snow–rain separation method for ATMS. The 2-min NMQ estimates are accumulated to match the hourly gauge observations (Fig. 3). Only NMQ observations with RQIs greater than 0.5 are included in the comparison. The correlation coefficient, RMSE, and bias are 0.65, 0.68 mm h^{-1}, and −2.9%, respectively. It appears that these two measurements agree reasonably well. More detailed comparisons (e.g., over different regions and for

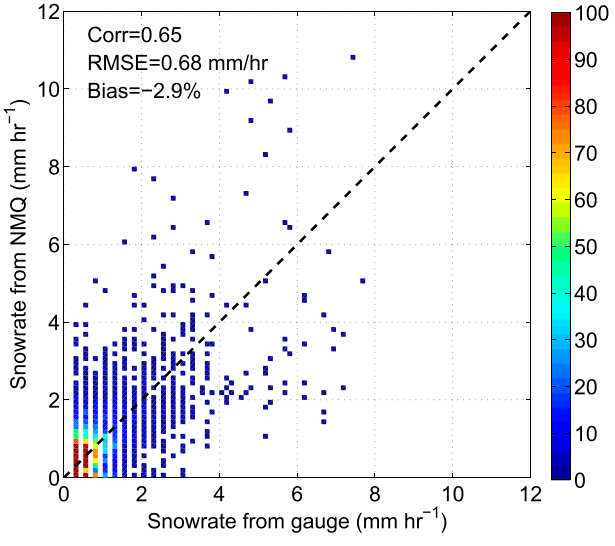

FIG. 3. Scatterplot between gauge-observed snowfall rate and NMQ snowfall rate over the CONUS in 2014 at about 482 first-order weather stations.

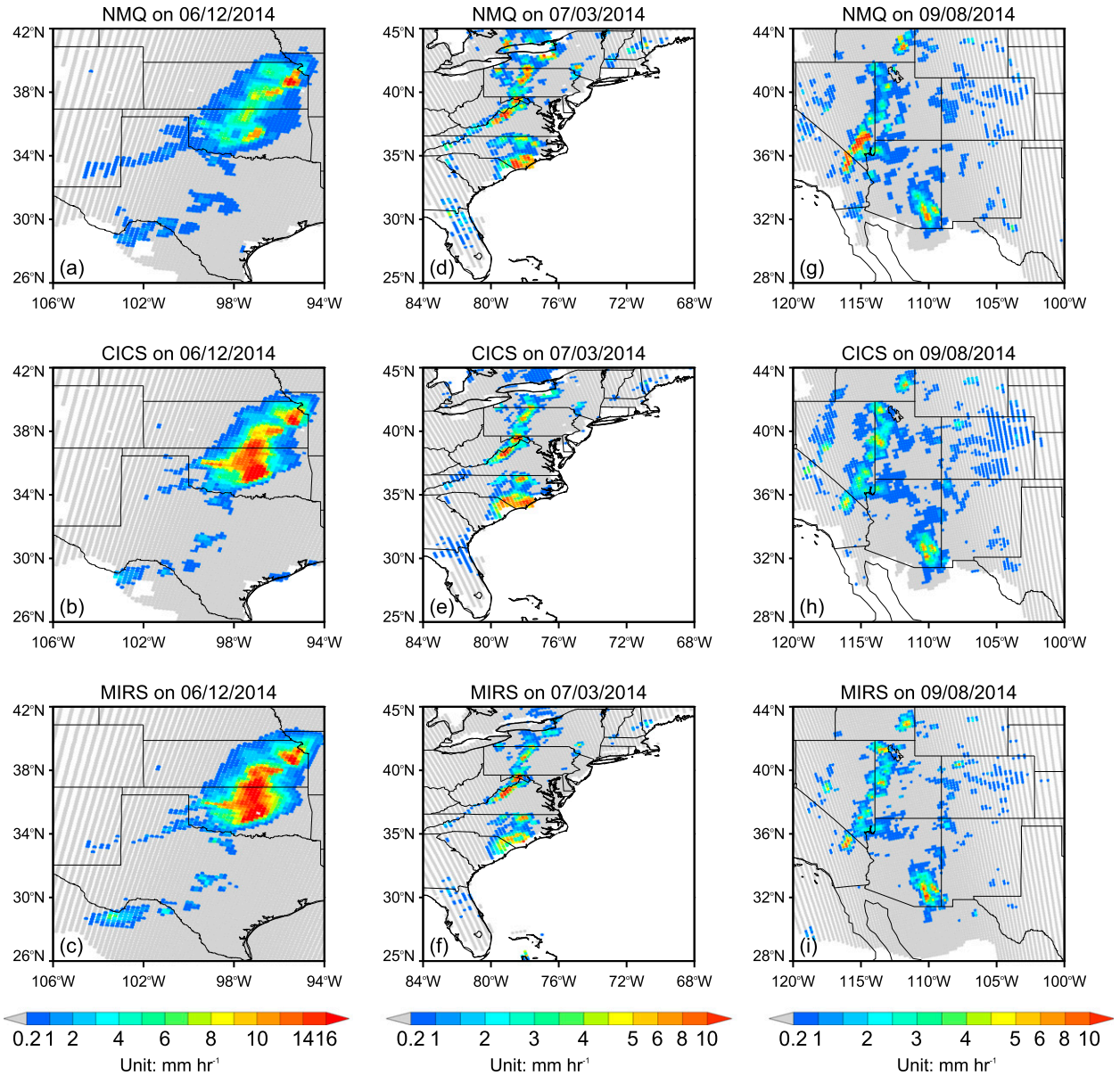

FIG. 4. Three rain cases on 12 Jun, 3 Jul, and 8 Sep 2014 (top) observed by NMQ, (middle) retrieved by our algorithm (CICS), and (bottom) retrieved by the MIRS algorithm.

different snow systems) are needed in the future. The purpose for this preliminary comparison is to demonstrate that the high-resolution NMQ snowfall observations largely agree with surface gauge observations and are therefore suitable to use to construct the snowfall database for the ATMS retrieval algorithm.

7. Precipitation retrieval results

In this section, the precipitation retrieval performance is demonstrated through case studies and statistical analysis for both rainfall and snowfall. The geospatial distribution of the precipitation over CONUS and over the 60°S–60°N land region derived from the CONUS database will also be shown.

a. Rainfall retrieval performance

1) CASE STUDIES

Three rain cases on 12 June, 3 July, and 8 September 2014 are selected (Figs. 4, 5). These three cases represent very different rainfall systems (deep convection, hurricane rainfall, and widespread stratiform) under different climate regimes. For the deep convection case over the

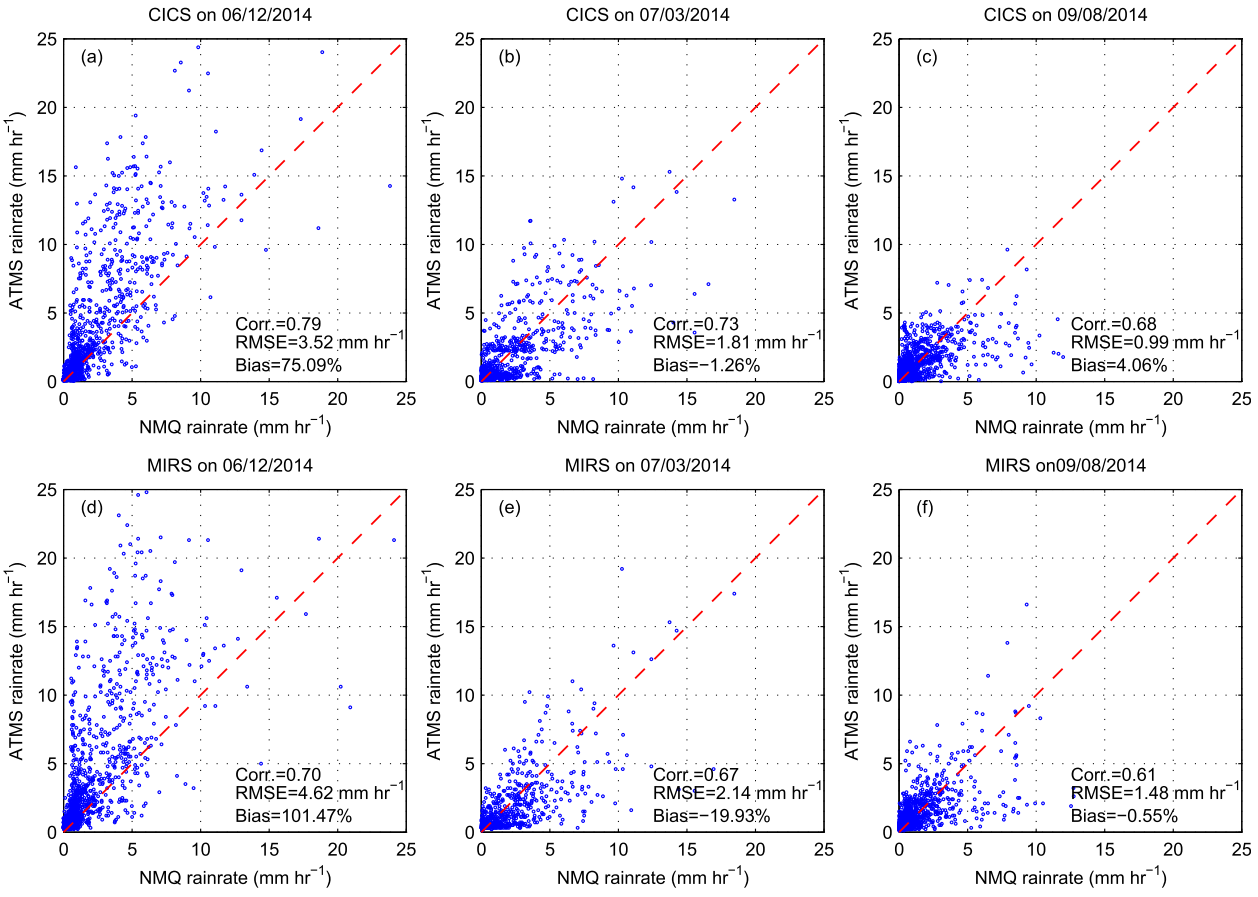

FIG. 5. Scatterplots between NMQ-observed rain rate and retrieved rain rate by our algorithm and MIRS algorithm for the three rain cases shown in Fig. 4.

central United States on 12 June 2014, the local weather office reported hail. Both our algorithm [denoted as Cooperative Institute for Climate and Satellites (CICS) in Figs. 4, 5] and MIRS capture the center of the convective cell (Figs. 4a–c). Compared to the NMQ observations, both algorithms overestimate the rainfall intensity in the center of the convective cell. This overestimation is alleviated in the CICS algorithm, which is more evident from the scatterplots (cf. Figs. 5a,d). The overestimation is a common issue for all passive microwave retrieval results when there exists a strong scattering signature but without proportional heavy surface rainfall. For the hurricane case, it is found that the heavy precipitation center is well captured by both algorithms. MIRS slightly underestimates the heavy rain over North Carolina. For the case over the western United States with arid background, both algorithms are able to detect the rainfall well. The CICS algorithm shows slightly better performance, indicated by a smaller RMSE and larger correlation coefficient (cf. Figs. 5c,f).

In summary, case studies demonstrated that the CICS algorithm can adequately capture the rainfall characteristics for different rainfall systems under different climate regimes. In addition, the CICS algorithm achieves a comparable performance relative to MIRS. The CICS algorithm is trained by the NMQ observations, which very likely accounts for the slightly larger correlation and smaller RMSE from the CICS algorithm in these three case studies.

2) OVERALL RAINFALL RETRIEVAL PERFORMANCE

The overall rainfall retrieval performance for the four seasons in 2014 is presented in Fig. 6. The correlation between the ATMS-retrieved rain rate and NMQ-observed rain rate is 0.67, 0.66, 0.65, and 0.71 for spring, summer, fall, and winter, respectively. The RMSEs are 1.98, 2.17, 1.62, and 1.22 mm h^{-1} for these four seasons. Additionally, overall the retrieved results in these four seasons are positively biased with biases at 31.19%, 17.32%, 10.44%, and 6.61% from spring to winter. Next, both rain rate and the one standard deviation corresponding to each retrieved rain rate are

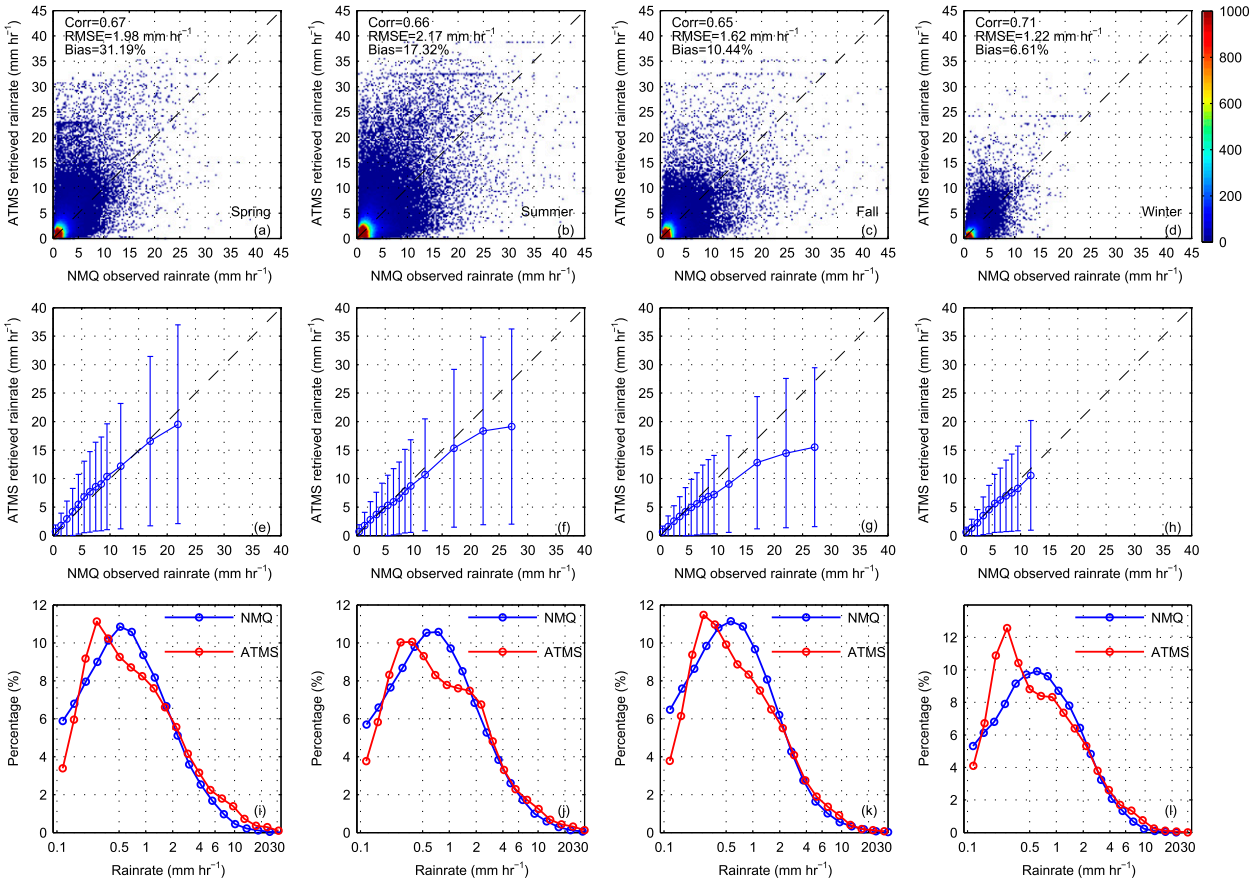

FIG. 6. (a)–(d) Scatterplots between NMQ-observed rain rate and ATMS-retrieved rain rate in spring, summer, fall, and winter of 2014, respectively. (e)–(h) The averaged NMQ and ATMS rain rate in several rain-rate bins (e.g., 0–0.5, 0.5–1.0, . . . , 25–30 mm h^{-1}) using data from (a)–(d). The corresponding averaged one-standard-deviation error bar in each small bin is overlapped. (i)–(l) The NMQ and ATMS rain-rate histograms from spring to winter. Note the x axis is on log-10 scale.

averaged in several small rain-rate bins (0–0.5, 0.5–1.0, . . . , 25–30 mm h^{-1}). The underestimation from the ATMS retrieval results is evident when the rain rate is larger than 15 mm h^{-1}, which is especially obvious in the summer and fall seasons (Figs. 6e–h). This underestimation is probably caused by the nonunique relation between surface precipitation and TB. In other words, the same TB signature can result from different combinations of surface background and precipitation profiles (Kummerow et al. 2011; You et al. 2011; You and Liu 2012). Because of this nonunique relation, heavy precipitation (e.g., precipitation greater than 15 mm h^{-1} in this work) is underestimated since some light precipitation possesses very similar TB signatures to that from heavy precipitation. Other possible reasons include the TB saturation due to heavy rainfall and the inherent uncertainty associated with the Bayesian retrieval (Seo et al. 2007). Despite the evident underestimation in the heavy precipitation scenario, the one-standard-deviation error bar covers the dynamic range of the NMQ-observed rain rate, which makes it a valuable uncertainty metric. As expected, the one standard deviation becomes larger as the rain-rate intensity increases. The histograms of the NMQ-observed rain rate and ATMS-retrieved rain rate agree well for rain rates larger than 1 mm h^{-1}, regardless of the seasons (Figs. 6i–l). For the rain rates less than 1 mm h^{-1}, large discrepancies exist, particularly in the winter season. These results are consistent with previous studies (e.g., Dinku et al. 2010; Laviola et al. 2013). It is clear from the ATMS rain-rate histogram that there are too many light rain-rate values (<1 mm h^{-1}). One of the reasons is that the larger FOV size over the edge requires averaging many more NMQ points to match the V88 resolution. By averaging more NMQ points, the mean rain-rate values are inevitably smaller. These relatively smaller values over the edge contribute to the retrieval result over the center.

The overall retrieval performance in 2014 agrees better near the center of the scan line (beam position

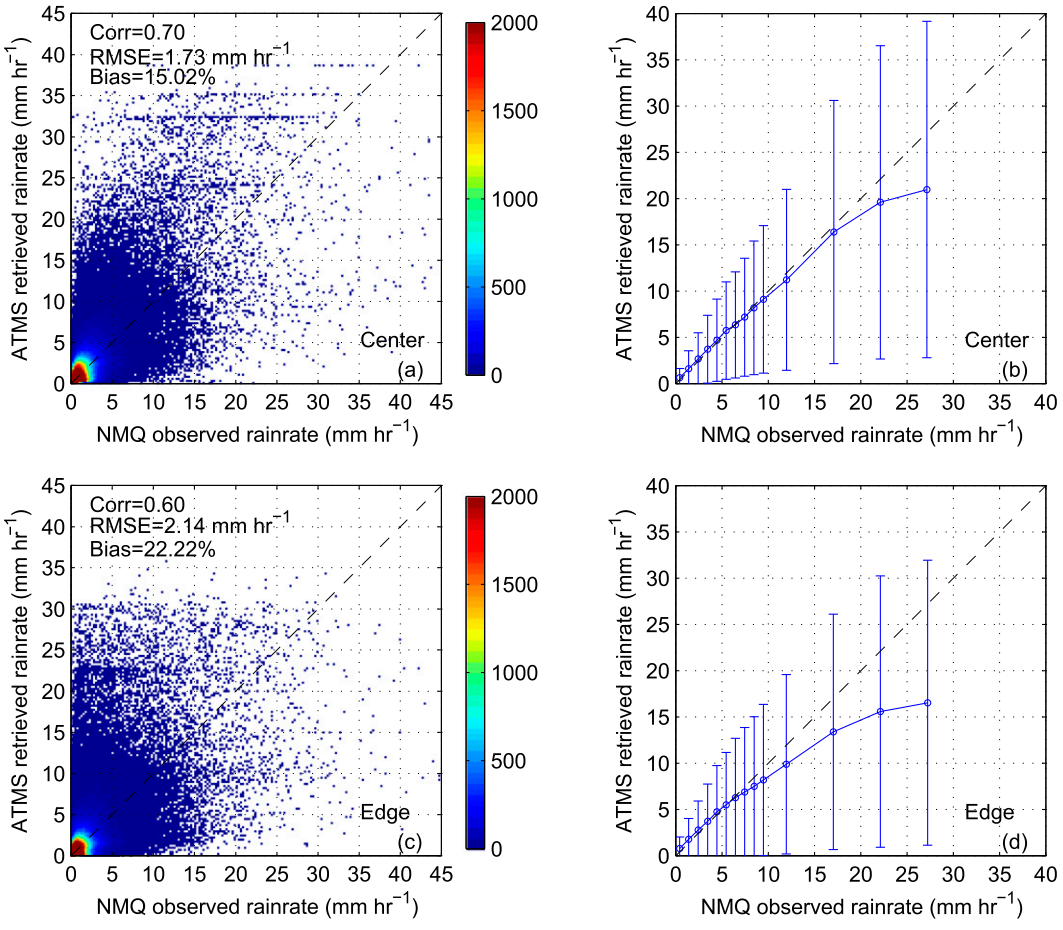

FIG. 7. (a) Scatterplot between NMQ-observed rain rate and ATMS-retrieved rain rate in 2014 over the center of the scan line (beam position from 21 to 76). (b) The averaged NMQ and ATMS rain rate in several rain-rate bins (e.g., 0–0.5, 0.5–1.0, . . . , 25–30 mm h^{-1}) using data from (a); the corresponding averaged one-standard-deviation error bar in each small bin is overlapped. (c) As in (a), but for values over the edge of the scan line (beam position from 1 to 20 and 77 to 96). (d) As in (b), but for values over the edge of the scan line (beam position from 1 to 20 and 77 to 96).

from 21 to 76) than that over the edge (beam position from 1 to 20 and 77 to 96), as indicated by larger correlation, smaller RMSE, and lower bias (Fig. 7). Comparing Fig. 7b with Fig. 7d, it is clear that retrievals at the edge of the swath underestimate rain rates more than near nadir for rain rates larger than 15 mm h^{-1}. Similar features are observed in the snowfall retrieval results. As mentioned above, the precipitation rate is smaller in the edge database because the larger FOV size requires averaging the NMQ field in a much larger area. Therefore, the heavy precipitation would be underestimated more severely over the edge if it indeed occurs. The larger variability of FOV size in the edge database also likely contributes to the larger underestimates over the edge. For example, the FOV size at beam position 21 is about 1.5 times larger than that at beam position 48 (at the very center). However, the FOV size at beam position 96 (at the very edge) is about 3 times larger than that at beam position 77.

3) GEOSPATIAL RAINFALL DISTRIBUTION OVER CONUS

The NMQ and ATMS rain rates are averaged into a 1° × 1° grid box to examine the average daily precipitation on seasonal scales (Fig. 8). To compare the retrieved results with those from NMQ, only the precipitation pixels with RQIs larger than 0.5 are considered for both rainfall and snowfall over CONUS.

For all seasons, all of the large-scale rainfall spatial patterns observed by NMQ are captured by the ATMS retrieval results, including the heavy rainfall close to the Gulf of Mexico in spring and heavy rainfall in the Florida Panhandle and in the central United States in summer. However, some differences also exist. For example, the daily ATMS rainfall is

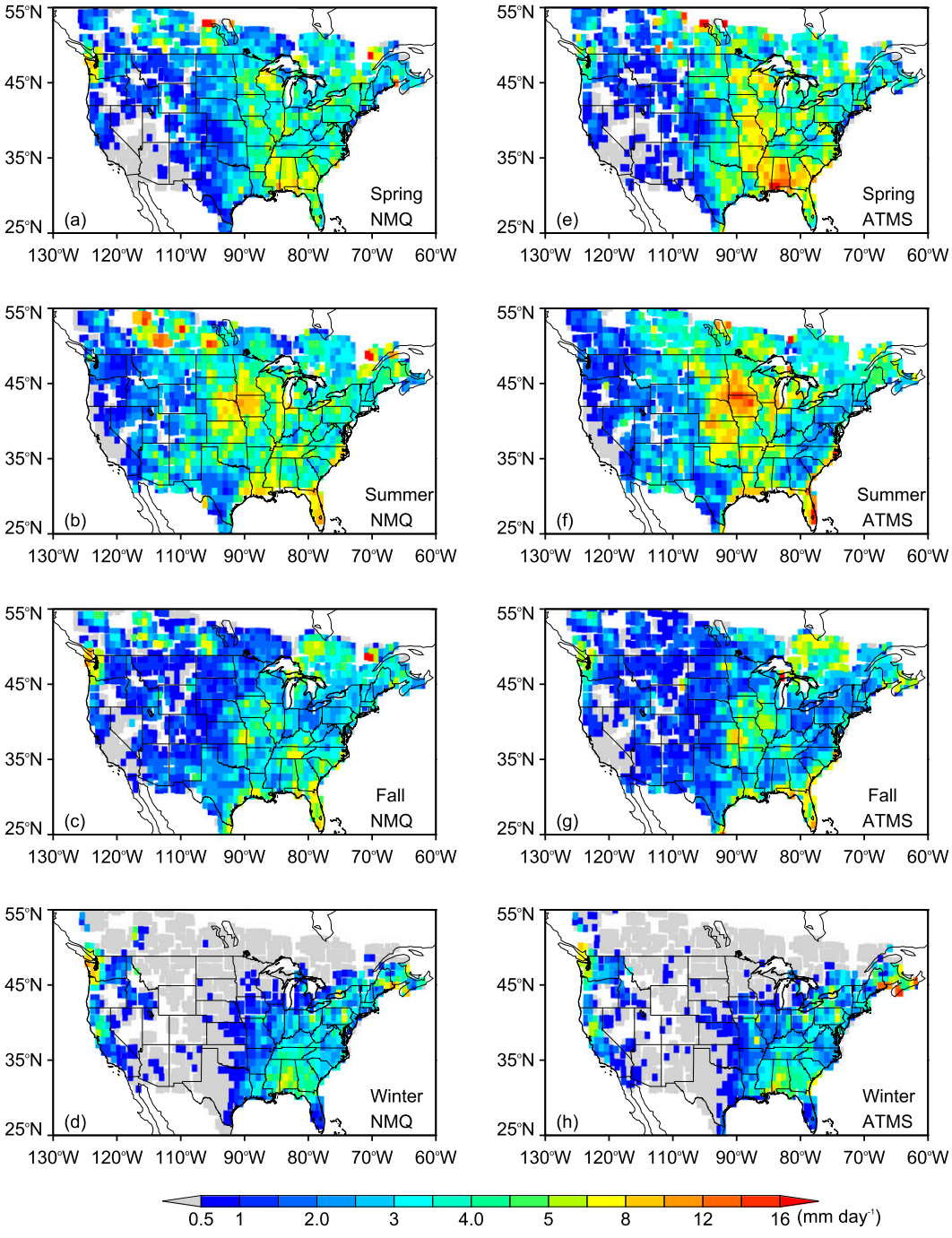

FIG. 8. (a)–(d) Geospatial distribution of NMQ-observed rain rate over CONUS from spring to winter of 2014. (e)–(h) Geospatial distribution of ATMS-retrieved rain rate over CONUS from spring to winter of 2014.

larger because ATMS estimates light rain more frequently than NMQ. The overestimation over the central United State in summer is also evident, which is caused by the stronger scattering signature (probably due to hail aloft) without producing proportional surface rain rate. The overestimate in winter over the northeast United States is likely caused by the snow-covered ground.

Overall, despite some regional discrepancies between the retrieved and observed rain rate, the geospatial pattern from the retrieved rain rate is largely consistent with that from the NMQ observations.

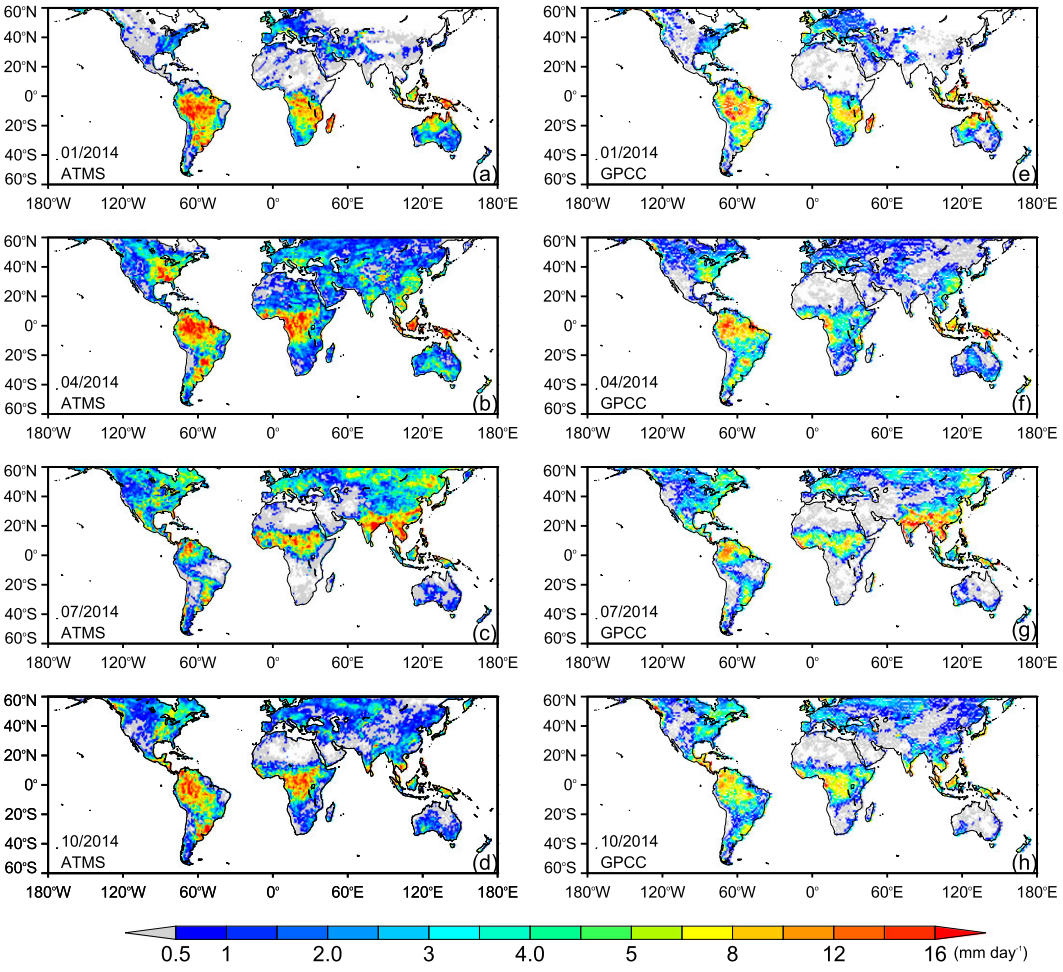

FIG. 9. (a)–(d) Geospatial distribution of the ATMS-retrieved rain rate over 60°S–60°N in January, April, July, and October 2014. (e)–(h) Geospatial distribution of the gauge-analysis (GPCC) rain rate over 60°S–60°N in January, April, July, and October 2014.

4) GEOSPATIAL RAINFALL DISTRIBUTION OVER 60°S–60°N

When developing a precipitation retrieval algorithm based on regional observations (CONUS in this study), a major concern is how to extend this algorithm to other areas. Here, the ATMS algorithm was run over land for 60°S–60°N using the database constructed by collocated NMQ and ATMS observations over CONUS. The same detection and retrieval procedure is applied to snowfall retrieval. The retrieved rain rates are averaged to 1° × 1° (Fig. 9). The result is compared with GPCC gauge-analysis rainfall in January, April, July, and October 2014. Since only the rainfall retrieval is discussed in this section, the GPCC snowfall observation is filtered out if there are no ATMS rainfall pixels in a certain grid box (e.g., Siberia in January 2014).

The progress and retreat of major rainbands over the tropical and subtropical regions [e.g., intertropical convergence zone (ITCZ) rainband and the monsoon rainfall over India and China] are well captured by the ATMS-retrieved results. Compared with the GPCC results, in general, the mean rain rate is larger. In January and April 2014, more rainfall is observed by ATMS over the Sahara Desert region, which is likely caused by the false detection by the passive microwave radiometer. Considering the independent data sources are used, that is, GPCC results are generated from gauge observations, while our results are based on CONUS radar observations, discrepancies between these two products are expected. Also, GPCC gauges continually measure daily accumulations, whereas ATMS has an instantaneous view at 0130 and 1330 local time, such that the precipitation diurnal cycle introduces an observation bias.

The completeness of the database also contributes to the discrepancy between GPCC and ATMS rain rates. To demonstrate this issue, the distribution of the TB at

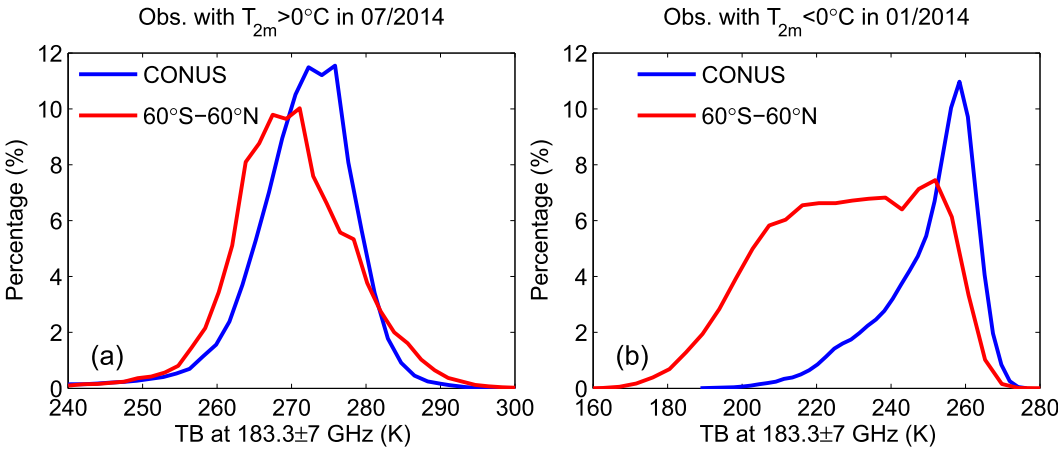

FIG. 10. (a) The TB at 183.3 ± 7 GHz over CONUS and the 60°S–60°N land region, except CONUS, in July 2014 with $T_{2m} > 0$°C. (b) The TB at 183.3 ± 7 GHz over CONUS and the 60°S–60°N land region, except CONUS, in January 2014 with $T_{2m} < 0$°C.

183.3 ± 7 GHz over CONUS and over the non-CONUS land portion of the 60°S–60°N region are shown in Fig. 10. The TB at 183.3 ± 7 GHz is chosen here purely for demonstration. TBs at other frequencies show a similar histogram distribution pattern. It is clear that the TB distribution over CONUS in July 2014 is not identical to that over the 60°S–60°N region, where the TB is slightly colder (Fig. 10a), which results in either false rainfall detection or rain-rate overestimation. Nevertheless, these two TB distributions are similar, which ensures that the major rainbands over the 60°S–60°N land region are captured. In contrast, the TB distributions over CONUS in January 2014 are dramatically different from those over the 60°S–60°N land region. Specifically, most of the TBs over the 60°S–60°N land region in winter are much colder than those over CONUS. This characteristic will cause many snowfall detection false alarms and large snowfall rate overestimations, which will be shown in the global snowfall retrieval results (Fig. 14, described in greater detail below).

In summary, it is demonstrated that only using the CONUS radar observations to construct the database to retrieve rain rate from ATMS can well capture the progress and retreat of the major rainbands (e.g., ITCZ). Discrepancies exist between ATMS retrieval results and GPCC gauge-analysis product because of the different data sources, the sampling frequency, and the database completeness issues.

b. *Snowfall retrieval performance*

The snowfall retrieval performance is demonstrated first through case studies, then the overall snowfall retrieval statistics are provided. Hourly automated snow observations from ISD surface reports in the Rocky Mountains area are also used to verify the snowfall detection performance.

1) CASE STUDIES AND OVERALL STATISTICS

Two snowfall cases are selected (Fig. 11), including the snowfall event over the Rocky Mountain region on 1 February 2014 and a heavy snowstorm over the New England region on 14 February 2014.

For the case over the Rocky Mountain region, ATMS detects a much broader snowfall occurrence area than the NMQ observations (Figs. 11a,b). Automated weather reports at the closest hour to the ATMS observations indicate the extent of the snowfall is reasonable. Evidently, the NMQ observations miss almost all the snowfall in the Rocky Mountain region because of the terrain blockage, while both the NMQ and ATMS capture the snow signature over the central United States. In terms of snowfall intensity, the correlation between the ATMS and NMQ is about 0.42 based on the pixels when both instruments detect snowfall in this case. For the New England region snow case (Figs. 11c,d), ATMS detects the center of the snowfall from Connecticut to New Hampshire, but severe underestimation is noticed in Maine and New Brunswick. In terms of snowfall intensity, for this case the correlation and RMSE are 0.62 and 0.80 mm h^{-1}, respectively.

Figure 12 displays the overall statistics for the snowfall retrieval results. The correlation, RMSE, and bias between the NMQ-observed snowfall rate and ATMS-retrieved snowfall rate are 0.41, 0.66 mm h^{-1}, and −15.02%, respectively (Fig. 12a). The underestimation of snowfall rate is evident throughout the

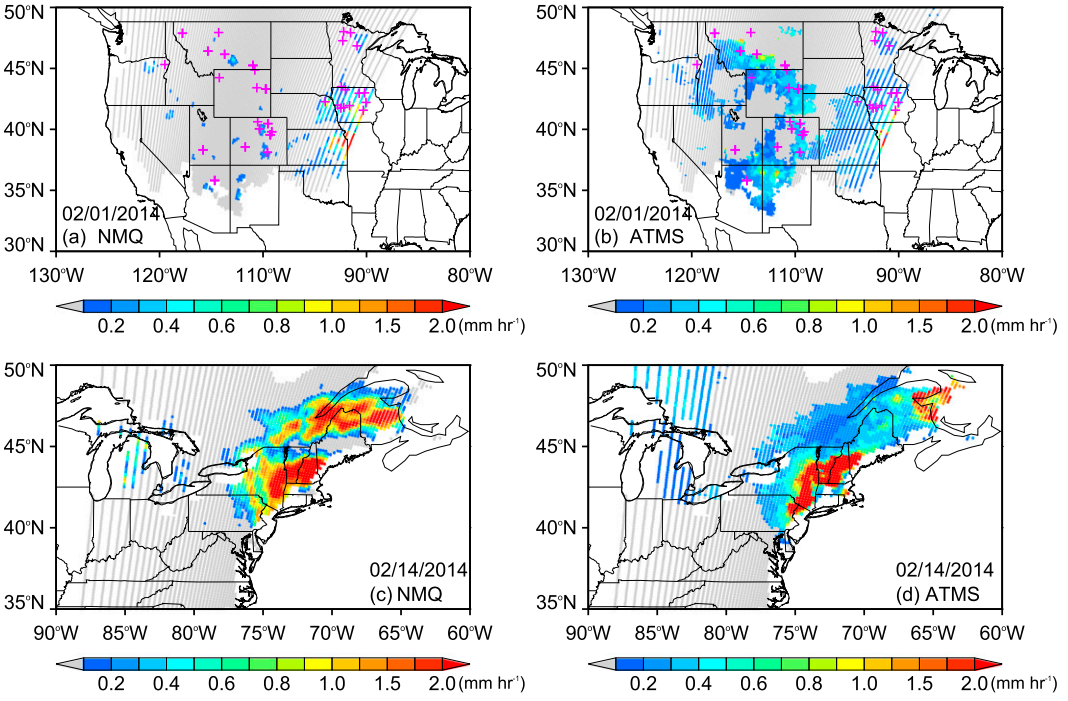

FIG. 11. (a) Snow event observed by NMQ on 1 Feb 2014 in the Rocky Mountain region. (b) As in (a), but for the retrieval by ATMS. The magenta plus signs represent the snow occurrence extracted from the ground automated weather reports. (c) Snow event observed by NMQ on 14 Feb 2014 in the New England region. (d) As in (c), but for the retrieval by ATMS.

snowfall range, which is likely due to surface contamination and weak scattering signatures from shallow snowfall events (Wang et al. 2013; Kongoli et al. 2015). The discrepancy between the NMQ and ATMS is further demonstrated by snowfall rate PDFs (Fig. 12c). Obviously, there is too much light snowfall in the retrieved snowfall results, which is responsible for the underestimation illustrated in Fig. 12b. Similar to rainfall retrieval results, this underestimation can be partially explained by the larger FOV size over the edge.

2) GEOSPATIAL SNOWFALL DISTRIBUTION OVER CONUS

The geospatial distribution of the NMQ-observed and ATMS-retrieved snowfall are shown in Fig. 13. In the calculation process, only the pixels with RQI greater than 0.5 are included. The most striking feature

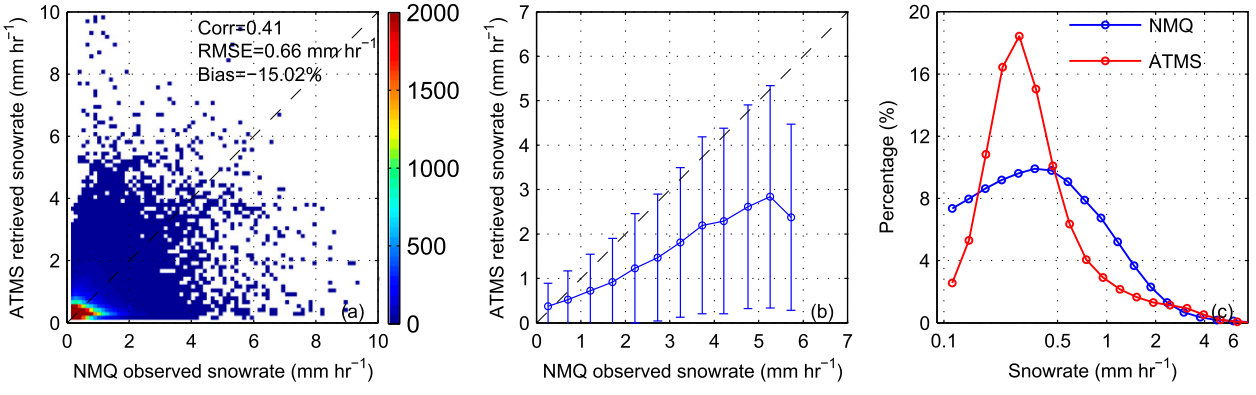

FIG. 12. (a) Scatterplot between NMQ-observed snowfall rate and ATMS-retrieved snowfall rate. (b) The averaged NMQ and ATMS snowfall rate in several snowfall rate bins (e.g., 0–0.2, 0.2–0.6, . . . , 6–10 mm h^{-1}) using data in (a). The corresponding averaged one-standard-deviation error bar in each small bin is added. (c) The snowfall rate histograms from ATMS and NMQ.

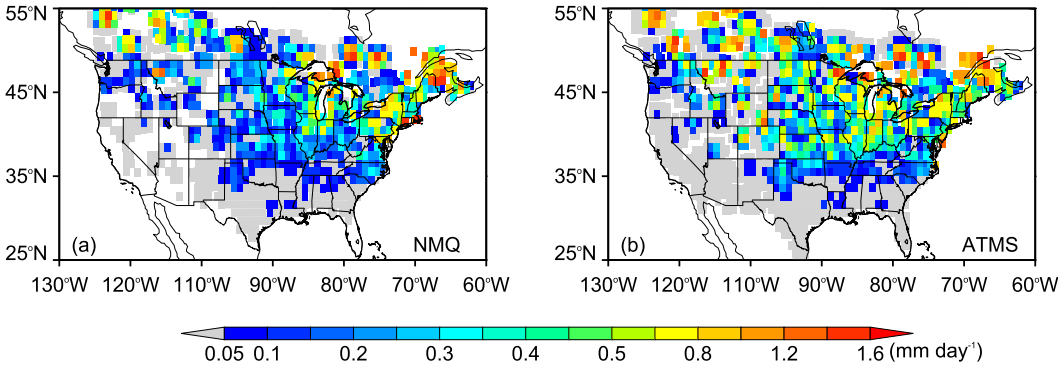

FIG. 13. (a) Geospatial distribution of the NMQ-observed snowfall rate over CONUS in 2014. (b) As in (a), but observed by ATMS.

is that NMQ misses almost the entire snow event in the Rocky Mountain region in Fig. 13a, which is demonstrated by the ground gauge observations (Durre et al. 2013). In contrast, the snowfall accumulation is evident in the Rocky Mountain region from the ATMS retrieval results. The snowfall pattern from the central to the eastern United States agrees fairly well between the NMQ observations and ATMS-retrieved results, with slightly overestimation from ATMS in the central United States.

Like the rainfall retrieval over the 60°S–60°N region, a similar procedure is applied to the ATMS-retrieved snowfall rate from January to April 2014. Only the results in January 2014 are shown in Fig. 14. The most evident feature is the artificially large retrieved snowfall rate over southeastern Canada, the Tibetan Plateau, and Siberia. This large snowfall rate overestimation is caused by the much colder TBs in these regions, which is illustrated in Fig. 10b for the TB distribution at 183.3 ± 7 GHz. The much colder TBs result in frequent snowfall detection false alarms and overestimations. The retrieved snowfall rate magnitude in western Europe seems reasonable, though independent ground observations are needed to verify this result.

8. Conclusions and discussion

Built upon a previously published algorithm for SSMIS (imager), a prototype precipitation algorithm for ATMS (sounder) using 3-yr coincident NMQ ground radar observations and ATMS observations over CONUS was developed. The major modifications to the SSMIS algorithm addressed the varying footprint size of ATMS pixels, the lack of error estimates associated with the retrieval, and the applicability of the algorithm to the near-global domain.

Three cases over CONUS demonstrate that this prototype algorithm is able to capture the major characteristics of these rainfall systems with correlation varying from 0.68 to 0.79. In these three cases, the algorithm achieved a comparable performance relative to MIRS. The correlation coefficient is about 0.66 for all four seasons, and the RMSE varies between 1.27 and 2.25 mm h^{-1}. The one-standard-deviation error bar well covered the dynamic range of the ground radar

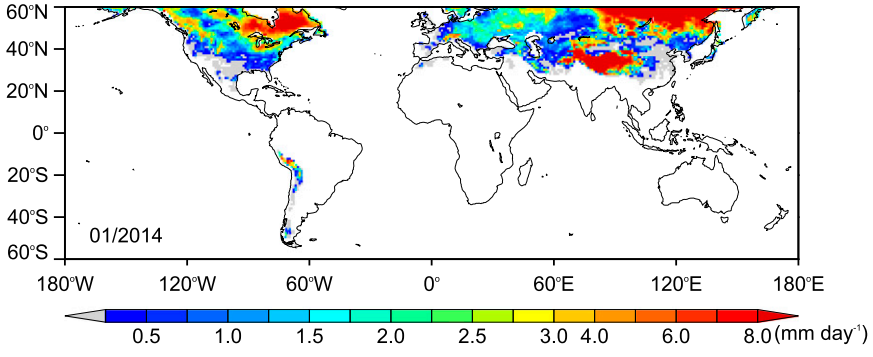

FIG. 14. Geospatial distribution of the ATMS-retrieved snowfall rate over 60°S–60°N in January 2014.

observations. A major improvement in this work is that the retrieval produces the uncertainty (variance) associated with each precipitation estimation. Like all passive microwave retrieval results, the heavy precipitation is underestimated because of the nonunique relation between rain rate and TBs. The geospatial pattern of the retrieved rain rate is largely consistent with that from NMQ observations; however, the magnitude often disagrees. For example, the heavy rainfall in the central United States and in the Florida Panhandle is well captured by both NMQ rain rate and ATMS-retrieved rain rate. ATMS overestimates rain rates over CONUS, which is primarily due to frequent false alarms of light rainfall from ATMS.

To demonstrate that this prototype algorithm can be extended to retrieve precipitation in other regions, precipitation rates are calculated over the 60°S–60°N belt. Although the databases are constructed by ground radar observations over CONUS, the annual movement of the major rainbands in tropical regions (e.g., ITCZ) and in midlatitudes (monsoon rainfall in India and China) is evident. The results are also consistent with the GPCC gauge-analysis product, although average daily rain rates are overestimated by ATMS. This overestimation is likely caused by the different data sources and database completeness issues. In this study, the ATMS retrieval results are trained using the NMQ ground radar observations, while the GPCC is a gauge-analysis product. For the database completeness problem, the TB at the 60°S–60°N land region is slightly colder than that over CONUS, which contributes to the overestimation. The satellite sample frequency issue (i.e., snapshot vs accumulation; Soman et al. 1995) may also contribute to the overestimation. Because of the preliminary nature of these results, a detailed evaluation of the retrieval results is needed on a global scale for algorithm improvement in the future.

For the snowfall retrieval performance, ATMS captured a snowfall event over the Rocky Mountain region, as demonstrated by ground gauge observations, while the NMQ observations almost entirely miss the snowfall event over that region. The snowfall pattern from the central to the eastern United States is well captured by the ATMS results, which largely agree with the NMQ observations. Similar to the rainfall retrieval, we also applied the snowfall retrieval algorithm to the land portion of the 60°S–60°N belt. Artificially large snowfall rates are obtained in southeastern Canada, the Tibetan Plateau, and Siberia. This is caused by the much colder TBs in these regions, which results in frequent snowfall detection false alarms and overestimations.

The satellite community is continuing to pursue new algorithms for precipitation retrievals for passive microwave sounders. For example, the Goddard profiling algorithm (GPROF) and the Global Satellite Mapping of Precipitation (GSMaP) are currently being adapted to retrieve the precipitation from sounders. Additionally, the snowfall detection/retrieval capability by passive microwave sensors continues to be researched. This study contributes to the field by introducing replicable techniques for rain–snow separation and precipitation retrievals from cross track–scanning radiometers.

Acknowledgments. NMQ data were provided by the National Severe Storms Laboratory (NSSL) of NOAA at Oklahoma (http://www.nssl.noaa.gov/contact.php). ATMS data were downloaded from NOAA Comprehensive Large Array-Data Stewardship System (CLASS; http://www.class.ngdc.noaa.gov). We thank four anonymous reviewers for their valuable suggestions and comments. Also, we thank Drs. Jun Dong, Isaac Moradi, Hu Yang, and Wenze Yang at the Earth System Science Interdisciplinary Center (ESSIC) for helpful discussions for the ATMS scanning scheme and the cloud filter. This research is supported by NOAA Grant NA09NES4400006.

REFERENCES

Aires, F., C. Prigent, F. Bernardo, C. Jiménez, R. Saunders, and P. Brunel, 2011: A Tool to Estimate Land-Surface Emissivities at Microwave frequencies (TELSEM) for use in numerical weather prediction. *Quart. J. Roy. Meteor. Soc.*, **137**, 690–699, doi:10.1002/qj.803.

Aonashi, K., and Coauthors, 2009: GSMaP passive microwave precipitation retrieval algorithm: Algorithm description and validation. *J. Meteor. Soc. Japan*, **87A**, 119–136, doi:10.2151/jmsj.87A.119.

Ashouri, H., K.-L. Hsu, S. Sorooshian, D. K. Braithwaite, K. R. Knapp, L. D. Cecil, B. R. Nelson, and O. P. Prat, 2015: PERSIANN-CDR: Daily precipitation climate data record from multisatellite observations for hydrological and climate studies. *Bull. Amer. Meteor. Soc.*, **96**, 69–83, doi:10.1175/BAMS-D-13-00068.1.

Auer, A. H., Jr., 1974: The rain versus snow threshold temperatures. *Weatherwise*, **27**, 67–67, doi:10.1080/00431672.1974.9931684.

Barrett, E., and M. Beaumont, 1994: Satellite rainfall monitoring: An overview. *Remote Sens. Rev.*, **11**, 23–48, doi:10.1080/02757259409532257.

Behrangi, A., H. Nguyen, B. Lambrigtsen, M. Schreier, and V. Dang, 2015: Investigating the role of multi-spectral and near surface temperature and humidity data to improve precipitation detection at high latitudes. *Atmos. Res.*, **163**, 2–12, doi:10.1016/j.atmosres.2014.10.019.

Boukabara, S.-A., and Coauthors, 2011: MiRS: An all-weather 1DVAR satellite data assimilation and retrieval system. *IEEE Trans. Geosci. Remote Sens.*, **49**, 3249–3272, doi:10.1109/TGRS.2011.2158438.

——, and Coauthors, 2013: A physical approach for a simultaneous retrieval of sounding, surface, hydrometeor, and cryospheric

parameters from *SNPP*/ATMS. *J. Geophys. Res. Atmos.*, **118**, 12 600–12 619, doi:10.1002/2013JD020448.

Bourgouin, P., 2000: A method to determine precipitation types. *Wea. Forecasting*, **15**, 583–592, doi:10.1175/1520-0434(2000)015<0583:AMTDPT>2.0.CO;2.

Chen, F. W., and D. H. Staelin, 2003: AIRS/AMSU/HSB precipitation estimates. *IEEE Trans. Geosci. Remote Sens.*, **41**, 410–417, doi:10.1109/TGRS.2002.808322.

Chen, S., and Coauthors, 2013: Evaluation and uncertainty estimation of NOAA/NSSL next-generation National Mosaic Quantitative Precipitation Estimation product (Q2) over the continental United States. *J. Hydrometeor.*, **14**, 1308–1322, doi:10.1175/JHM-D-12-0150.1.

Chiu, J. C., and G. W. Petty, 2006: Bayesian retrieval of complete posterior PDFs of oceanic rain rate from microwave observations. *J. Appl. Meteor. Climatol.*, **45**, 1073–1095, doi:10.1175/JAM2392.1.

Dai, A., 2008: Temperature and pressure dependence of the rain–snow phase transition over land and ocean. *Geophys. Res. Lett.*, **35**, L12802, doi:10.1029/2008GL033295.

——, I. Y. Fung, and A. D. Del Genio, 1997: Surface observed global land precipitation variations during 1900–88. *J. Climate*, **10**, 2943–2962, doi:10.1175/1520-0442(1997)010<2943:SOGLPV>2.0.CO;2.

Ding, B., K. Yang, J. Qin, L. Wang, Y. Chen, and X. He, 2014: The dependence of precipitation types on surface elevation and meteorological conditions and its parameterization. *J. Hydrol.*, **513**, 154–163, doi:10.1016/j.jhydrol.2014.03.038.

Dinku, T., F. Ruiz, S. J. Connor, and P. Ceccato, 2010: Validation and intercomparison of satellite rainfall estimates over Colombia. *J. Appl. Meteor. Climatol.*, **49**, 1004–1014, doi:10.1175/2009JAMC2260.1.

Durre, I., M. F. Squires, R. S. Vose, X. Yin, A. Arguez, and S. Applequist, 2013: NOAA's 1981–2010 U.S. climate normals: Monthly precipitation, snowfall, and snow depth. *J. Appl. Meteor. Climatol.*, **52**, 2377–2395, doi:10.1175/JAMC-D-13-051.1.

Ebtehaj, A. M., R. L. Bras, and E. Foufoula-Georgiou, 2015: Shrunken locally linear embedding for passive microwave retrieval of precipitation. *IEEE Trans. Geosci. Remote Sens.*, **53**, 3720–3736, doi:10.1109/TGRS.2014.2382436.

Evans, K. F., J. Turk, T. Wong, and G. L. Stephens, 1995: A Bayesian approach to microwave precipitation profile retrieval. *J. Appl. Meteor.*, **34**, 260–279, doi:10.1175/1520-0450-34.1.260.

——, S. J. Walter, A. J. Heymsfield, and G. M. McFarquhar, 2002: Submillimeter-wave cloud ice radiometer: Simulations of retrieval algorithm performance. *J. Geophys. Res.*, **107**, 4028, doi:10.1029/2001JD000709.

Ferraro, R. R., and G. F. Marks, 1995: The development of SSM/I rain-rate retrieval algorithms using ground-based radar measurements. *J. Atmos. Oceanic Technol.*, **12**, 755–770, doi:10.1175/1520-0426(1995)012<0755:TDOSRR>2.0.CO;2.

——, F. Weng, N. C. Grody, and L. Zhao, 2000: Precipitation characteristics over land from the *NOAA-15* AMSU sensor. *Geophys. Res. Lett.*, **27**, 2669–2672, doi:10.1029/2000GL011665.

——, and Coauthors, 2005: NOAA operational hydrological products derived from the Advanced Microwave Sounding Unit. *IEEE Trans. Geosci. Remote Sens.*, **43**, 1036–1049, doi:10.1109/TGRS.2004.843249.

Fisher, B., and D. B. Wolff, 2011: Satellite sampling and retrieval errors in regional monthly rain estimates from TMI, AMSR-E, SSM/I, AMSU-B, and the TRMM PR. *J. Appl. Meteor. Climatol.*, **50**, 994–1023, doi:10.1175/2010JAMC2487.1.

Gopalan, K., N.-Y. Wang, R. Ferraro, and C. Liu, 2010: Status of the TRMM 2A12 land precipitation algorithm. *J. Atmos. Oceanic Technol.*, **27**, 1343–1354, doi:10.1175/2010JTECHA1454.1.

Grody, N. C., 1991: Classification of snow cover and precipitation using the Special Sensor Microwave Imager. *J. Geophys. Res.*, **96**, 7423–7435, doi:10.1029/91JD00045.

——, 1993: Remote sensing of the atmosphere from satellites using microwave radiometry. *Atmospheric Remote Sensing by Microwave Radiometry*, M. A. Janssen, Ed., Wiley Series in Remote Sensing and Image Processing, Vol. 6, Wiley, 259–334.

——, J. Zhao, R. Ferraro, F. Weng, and R. Boers, 2001: Determination of precipitable water and cloud liquid water over oceans from the *NOAA 15* advanced microwave sounding unit. *J. Geophys. Res.*, **106**, 2943–2953, doi:10.1029/2000JD900616.

Hastings, D. A., and P. Dunbar, 1998: Development and assessment of the Global Land One-km Base Elevation Digital Elevation Model (GLOBE). *Proc. Int. Society of Photogrammetry and Remote Sensing Commission IV Symp.*, Stuttgart, Germany, ISPRS, 218–221.

Hou, A. Y., and Coauthors, 2014: The Global Precipitation Measurement Mission. *Bull. Amer. Meteor. Soc.*, **95**, 701–722, doi:10.1175/BAMS-D-13-00164.1.

Huffman, G. J., and Coauthors, 2007: The TRMM Multisatellite Precipitation Analysis (TMPA): Quasi-global, multiyear, combined-sensor precipitation estimates at fine scales. *J. Hydrometeor.*, **8**, 38–55, doi:10.1175/JHM560.1.

Islam, T., P. K. Srivastava, Q. Dai, M. Gupta, and L. Zhuo, 2015: Rain rate retrieval algorithm for conical-scanning microwave imagers aided by random forest, RReliefF, and Multivariate Adaptive Regression Splines (RAMARS). *IEEE Sens. J.*, **15**, 2186–2193, doi:10.1109/JSEN.2014.2372814.

Joyce, R. J., J. E. Janowiak, P. A. Arkin, and P. Xie, 2004: CMORPH: A method that produces global precipitation estimates from passive microwave and infrared data at high spatial and temporal resolution. *J. Hydrometeor.*, **5**, 487–503, doi:10.1175/1525-7541(2004)005<0487:CAMTPG>2.0.CO;2.

Kidd, C., and V. Levizzani, 2011: Status of satellite precipitation retrievals. *Hydrol. Earth Syst. Sci.*, **15**, 1109–1116, doi:10.5194/hess-15-1109-2011.

Kim, E., C.-H. J. Lyu, K. Anderson, R. V. Leslie, and W. J. Blackwell, 2014: *S-NPP* ATMS instrument prelaunch and on-orbit performance evaluation. *J. Geophys. Res. Atmos.*, **119**, 5653–5670, doi:10.1002/2013JD020483.

Kim, M.-J., J. Weinman, W. Olson, D.-E. Chang, G. Skofronick-Jackson, and J. Wang, 2008: A physical model to estimate snowfall over land using AMSU-B observations. *J. Geophys. Res.*, **113**, D09201, doi:10.1029/2007JD008589.

Kongoli, C., P. Pellegrino, R. R. Ferraro, N. C. Grody, and H. Meng, 2003: A new snowfall detection algorithm over land using measurements from the Advanced Microwave Sounding Unit (AMSU). *Geophys. Res. Lett.*, **30**, 1756, doi:10.1029/2003GL017177.

——, H. Meng, J. Dong, and R. Ferraro, 2015: A snowfall detection algorithm over land utilizing high-frequency passive microwave measurements—Application to ATMS. *J. Geophys. Res. Atmos.*, **120**, 1918–1932, doi:10.1002/2014JD022427.

Kubota, T., and Coauthors, 2007: Global precipitation map using satellite-borne microwave radiometers by the GSMaP project: Production and validation. *IEEE Trans. Geosci. Remote Sens.*, **45**, 2259–2275, doi:10.1109/TGRS.2007.895337.

Kummerow, C. D., W. S. Olson, and L. Giglio, 1996: A simplified scheme for obtaining precipitation and vertical hydrometeor

profiles from passive microwave sensors. *IEEE Trans. Geosci. Remote Sens.*, **34**, 1213–1232, doi:10.1109/36.536538.

——, and Coauthors, 2001: The evolution of the Goddard Profiling Algorithm (GPROF) for rainfall estimation from passive microwave sensors. *J. Appl. Meteor.*, **40**, 1801–1820, doi:10.1175/1520-0450(2001)040<1801:TEOTGP>2.0.CO;2.

——, S. Ringerud, J. Crook, D. Randel, and W. Berg, 2011: An observationally generated a priori database for microwave rainfall retrievals. *J. Atmos. Oceanic Technol.*, **28**, 113–130, doi:10.1175/2010JTECHA1468.1.

——, D. L. Randel, M. Kulie, N.-Y. Wang, R. Ferraro, S. Joseph Munchak, and V. Petkovic, 2015: The evolution of the Goddard Profiling Algorithm to a fully parametric scheme. *J. Atmos. Oceanic Technol.*, **32**, 2265–2280, doi:10.1175/JTECH-D-15-0039.1.

Laviola, S., and V. Levizzani, 2011: The 183-WSL fast rain rate retrieval algorithm: Part I: Retrieval design. *Atmos. Res.*, **99**, 443–461, doi:10.1016/j.atmosres.2010.11.013.

——, ——, E. Cattani, and C. Kidd, 2013: The 183-WSL fast rain rate retrieval algorithm. Part II: Validation using ground radar measurements. *Atmos. Res.*, **134**, 77–86, doi:10.1016/j.atmosres.2013.07.013.

Lin, X., and A. Y. Hou, 2008: Evaluation of coincident passive microwave rainfall estimates using TRMM PR and ground measurements as references. *J. Appl. Meteor. Climatol.*, **47**, 3170–3187, doi:10.1175/2008JAMC1893.1.

Linden, R., A. H. Fink, and R. Redl, 2015: Satellite-based climatology of low-level continental clouds in southern West Africa during the summer monsoon season. *J. Geophys. Res. Atmos.*, **120**, 1186–1201, doi:10.1002/2014JD022614.

Liu, G., and J. A. Curry, 1992: Retrieval of precipitation from satellite microwave measurement using both emission and scattering. *J. Geophys. Res.*, **97**, 9959–9974, doi:10.1029/92JD00289.

——, and E.-K. Seo, 2013: Detecting snowfall over land by satellite high-frequency microwave observations: The lack of scattering signature and a statistical approach. *J. Geophys. Res. Atmos.*, **118**, 1376–1387, doi:10.1002/jgrd.50172.

McCollum, J. R., and R. R. Ferraro, 2003: Next generation of NOAA/NESDIS TMI, SSM/I, and AMSR-E microwave land rainfall algorithms. *J. Geophys. Res.*, **108**, 8382, doi:10.1029/2001JD001512.

Moradi, I., B. Soden, R. Ferraro, P. Arkin, and H. Vömel, 2013: Assessing the quality of humidity measurements from global operational radiosonde sensors. *J. Geophys. Res. Atmos.*, **118**, 8040–8053, doi:10.1002/jgrd.50589.

Noh, Y.-J., G. Liu, E.-K. Seo, J. R. Wang, and K. Aonashi, 2006: Development of a snowfall retrieval algorithm at high microwave frequencies. *J. Geophys. Res.*, **111**, D22216, doi:10.1029/2005JD006826.

Petty, G. W., 1994: Physical retrievals of over-ocean rain rate from multichannel microwave imagery. Part II: Algorithm implementation. *Meteor. Atmos. Phys.*, **54**, 101–121, doi:10.1007/BF01030054.

——, 1995: The status of satellite-based rainfall estimation over land. *Remote Sens. Environ.*, **51**, 125–137, doi:10.1016/0034-4257(94)00070-4.

——, and K. Li, 2013: Improved passive microwave retrievals of rain rate over land and ocean. Part II: Validation and intercomparison. *J. Atmos. Oceanic Technol.*, **30**, 2509–2526, doi:10.1175/JTECH-D-12-00184.1.

Qiu, S., P. Pellegrino, R. Ferraro, and L. Zhao, 2005: The improved AMSU rain-rate algorithm and its evaluation for a cool season event in the western United States. *Wea. Forecasting*, **20**, 761–774, doi:10.1175/WAF880.1.

Sanò, P., D. Casella, A. Mugnai, G. Schiavon, E. A. Smith, and G. J. Tripoli, 2013: Transitioning from CRD to CDRD in Bayesian retrieval of rainfall from satellite passive microwave measurements: Part 1. Algorithm description and testing. *IEEE Trans. Geosci. Remote Sens.*, **51**, 4119–4143, doi:10.1109/TGRS.2012.2227332.

——, G. Panegrossi, D. Casella, F. Di Paola, L. Milani, A. Mugnai, M. Petracca, and S. Dietrich, 2015: The Passive Microwave Neural Network Precipitation Retrieval (PNPR) algorithm for AMSU/MHS observations: Description and application to European case studies. *Atmos. Meas. Tech.*, **8**, 837–857, doi:10.5194/amt-8-837-2015.

Schneider, U., A. Becker, P. Finger, A. Meyer-Christoffer, M. Ziese, and B. Rudolf, 2014: GPCC's new land surface precipitation climatology based on quality-controlled in situ data and its role in quantifying the global water cycle. *Theor. Appl. Climatol.*, **115**, 15–40, doi:10.1007/s00704-013-0860-x.

Seo, E.-K., and G. Liu, 2005: Retrievals of cloud ice water path by combining ground cloud radar and satellite high-frequency microwave measurements near the ARM SGP site. *J. Geophys. Res.*, **110**, D14203, doi:10.1029/2004JD005727.

——, ——, and K.-Y. Kim, 2007: A note on systematic errors in Bayesian retrieval algorithms. *J. Meteor. Soc. Japan*, **85**, 69–74, doi:10.2151/jmsj.85.69.

——, B.-J. Sohn, G. Liu, G.-H. Ryu, and H.-J. Han, 2008: Improvement of microwave rainfall retrievals in Bayesian retrieval algorithms. *J. Meteor. Soc. Japan*, **86**, 405–409, doi:10.2151/jmsj.86.405.

Sims, E. M., and G. Liu, 2015: A parameterization of the probability of snow–rain transition. *J. Hydrometeor.*, **16**, 1466–1477, doi:10.1175/JHM-D-14-0211.1.

Smith, A., N. Lott, and R. Vose, 2011: The integrated surface database: Recent developments and partnerships. *Bull. Amer. Meteor. Soc.*, **92**, 704–708, doi:10.1175/2011BAMS3015.1.

Soman, V. V., J. B. Valdés, and G. R. North, 1995: Satellite sampling and the diurnal cycle statistics of Darwin rainfall data. *J. Appl. Meteor.*, **34**, 2481–2490, doi:10.1175/1520-0450(1995)034<2481:SSATDC>2.0.CO;2.

Spencer, R. W., H. M. Goodman, and R. E. Hood, 1989: Precipitation retrieval over land and ocean with the SSM/I: Identification and characteristics of the scattering signal. *J. Atmos. Oceanic Technol.*, **6**, 254–273, doi:10.1175/1520-0426(1989)006<0254:PROLAO>2.0.CO;2.

Staelin, D. H., and F. W. Chen, 2000: Precipitation observations near 54 and 183 GHz using the *NOAA-15* satellite. *IEEE Trans. Geosci. Remote Sens.*, **38**, 2322–2332, doi:10.1109/36.868889.

Surussavadee, C., and D. H. Staelin, 2008a: Global millimeter-wave precipitation retrievals trained with a cloud-resolving numerical weather prediction model, Part I: Retrieval design. *IEEE Trans. Geosci. Remote Sens.*, **46**, 99–108, doi:10.1109/TGRS.2007.908302.

——, and ——, 2008b: Global millimeter-wave precipitation retrievals trained with a cloud-resolving numerical weather-prediction model, Part II: Performance evaluation. *IEEE Trans. Geosci. Remote Sens.*, **46**, 109–118, doi:10.1109/TGRS.2007.908299.

——, and ——, 2010: NPOESS precipitation retrievals using the ATMS passive microwave spectrometer. *IEEE Geosci. Remote Sens. Lett.*, **7**, 440–444, doi:10.1109/LGRS.2009.2038614.

Tang, L., Y. Tian, and X. Lin, 2014: Validation of precipitation retrievals over land from satellite-based passive microwave sensors. *J. Geophys. Res. Atmos.*, **119**, 4546–4567, doi:10.1002/2013JD020933.

Turk, F. J., Z. S. Haddad, and Y. You, 2014: Principal components of multifrequency microwave land surface emissivities. Part I: Estimation under clear and precipitating conditions. *J. Hydrometeor.*, **15**, 3–19, doi:10.1175/JHM-D-13-08.1.

Vila, D., R. Ferraro, and R. Joyce, 2007: Evaluation and improvement of AMSU precipitation retrievals. *J. Geophys. Res.*, **112**, D20119, doi:10.1029/2007JD008617.

Viltard, N., C. Burlaud, and C. D. Kummerow, 2006: Rain retrieval from TMI brightness temperature measurements using a TRMM PR-based database. *J. Appl. Meteor. Climatol.*, **45**, 455–466, doi:10.1175/JAM2346.1.

Vose, R. S., and Coauthors, 2014: Monitoring and understanding changes in extremes: Extratropical storms, winds, and waves. *Bull. Amer. Meteor. Soc.*, **95**, 377–386, doi:10.1175/BAMS-D-12-00162.1.

Wagner, J., 1957: Mean temperature from 1000 mb to 500 mb as a predictor of precipitation type. *Bull. Amer. Meteor. Soc.*, **10**, 584–590.

Wang, N.-Y., C. Liu, R. Ferraro, D. Wolff, E. Zipser, and C. Kummerow, 2009: TRMM 2A12 land precipitation product-status and future plans. *J. Meteor. Soc. Japan*, **87A**, 237–253, doi:10.2151/jmsj.87A.237.

Wang, Y., G. Liu, E.-K. Seo, and Y. Fu, 2013: Liquid water in snowing clouds: Implications for satellite remote sensing of snowfall. *Atmos. Res.*, **131**, 60–72, doi:10.1016/j.atmosres.2012.06.008.

Weng, F., L. Zhao, R. R. Ferraro, G. Poe, X. Li, and N. C. Grody, 2003: Advanced microwave sounding unit cloud and precipitation algorithms. *Radio Sci.*, **38**, 8068, doi:10.1029/2002RS002679.

Wolff, D. B., and B. L. Fisher, 2009: Assessing the relative performance of microwave-based satellite rain-rate retrievals using TRMM ground validation data. *J. Appl. Meteor. Climatol.*, **48**, 1069–1099, doi:10.1175/2008JAMC2127.1.

Wu, W., D. Kitzmiller, and S. Wu, 2012: Evaluation of radar precipitation estimates from the National Mosaic and Multisensor Quantitative Precipitation Estimation system and the WSR-88D precipitation processing system over the conterminous United States. *J. Hydrometeor.*, **13**, 1080–1093, doi:10.1175/JHM-D-11-064.1.

Yang, W., H. Meng, R. R. Ferraro, I. Moradi, and C. Devaraj, 2013: Cross-scan asymmetry of AMSU-A window channels: Characterization, correction, and verification. *IEEE Trans. Geosci. Remote Sens.*, **51**, 1514–1530, doi:10.1109/TGRS.2012.2211884.

Ye, H., J. Cohen, and M. Rawlins, 2013: Discrimination of solid from liquid precipitation over northern Eurasia using surface atmospheric conditions. *J. Hydrometeor.*, **14**, 1345–1355, doi:10.1175/JHM-D-12-0164.1.

Yong, B., D. Liu, J. J. Gourley, Y. Tian, G. J. Huffman, L. Ren, and Y. Hong, 2015: Global view of real-time TRMM Multisatellite Precipitation Analysis: Implications for its successor Global Precipitation Measurement mission. *Bull. Amer. Meteor. Soc.*, **96**, 283–296, doi:10.1175/BAMS-D-14-00017.1.

You, Y., and G. Liu, 2012: The relationship between surface rainrate and water paths and its implications to satellite rainrate retrieval. *J. Geophys. Res.*, **117**, D13207, doi:10.1029/2012JD017662.

——, ——, Y. Wang, and J. Cao, 2011: On the sensitivity of Tropical Rainfall Measuring Mission (TRMM) Microwave Imager channels to overland rainfall. *J. Geophys. Res.*, **116**, D12203, doi:10.1029/2010JD015345.

——, N.-Y. Wang, and R. Ferraro, 2015: A prototype precipitation retrieval algorithm over land using passive microwave observations stratified by surface condition and precipitation vertical structure. *J. Geophys. Res. Atmos.*, **120**, 5295–5315, doi:10.1002/2014JD022534.

Zhang, J., Y. Qi, K. Howard, C. Langston, and B. Kaney, 2011a: Radar quality index (RQI): A combined measure of beam blockage and VPR effects in a national network. *IAHS Publ.*, **351**, 388–393.

——, and Coauthors, 2011b: National Mosaic and Multi-Sensor QPE (NMQ) system: Description, results, and future plans. *Bull. Amer. Meteor. Soc.*, **92**, 1321–1338, doi:10.1175/2011BAMS-D-11-00047.1.